

Spring 5-1-2017

# Magmatic Hydrothermal Alteration and Secondary Post-Shock Features in Martian Olivine-Phyric Basalt Northwest Africa 10416; Petrology and Geochemistry of Primitive Achondrite Northwest Africa 11042

Zoltan Vaci

Follow this and additional works at: [https://digitalrepository.unm.edu/eps\\_etds](https://digitalrepository.unm.edu/eps_etds)

 Part of the [Cosmochemistry Commons](#), [Geochemistry Commons](#), [Geology Commons](#), and the [Volcanology Commons](#)

---

## Recommended Citation

Vaci, Zoltan. "Magmatic Hydrothermal Alteration and Secondary Post-Shock Features in Martian Olivine-Phyric Basalt Northwest Africa 10416; Petrology and Geochemistry of Primitive Achondrite Northwest Africa 11042." (2017).  
[https://digitalrepository.unm.edu/eps\\_etds/196](https://digitalrepository.unm.edu/eps_etds/196)

This Thesis is brought to you for free and open access by the Electronic Theses and Dissertations at UNM Digital Repository. It has been accepted for inclusion in Earth and Planetary Sciences ETDs by an authorized administrator of UNM Digital Repository. For more information, please contact [disc@unm.edu](mailto:disc@unm.edu).

Magmatic Hydrothermal Alteration and Secondary Post-Shock Features in Martian Olivine-  
Phyric Basalt Northwest Africa 10416;  
Petrology and Geochemistry of Primitive Achondrite Northwest Africa 11042

Zoltan Vaci

Bachelor of Science Geology

Rutgers University

THESIS

Submitted in partial fulfillment of the requirements for the degree of

Master of Science

Earth and Planetary Sciences

University of New Mexico,

Albuquerque, NM

July 2017



## Table of Contents

### **Part A: Magmatic Hydrothermal Alteration and Secondary Post-Shock Features in Martian**

|   |    |
|---|----|
| Olivine-Phyric Basalt Northwest Africa 10416..... | 1  |
| Abstract.....                                     | 1  |
| 1.0 Introduction.....                             | 1  |
| 2.0 Methods.....                                  | 3  |
| 3.0 Results.....                                  | 4  |
| 4.0 Discussion.....                               | 7  |
| 5.0 Conclusions.....                              | 12 |
| 6.0 Figures.....                                  | 14 |
| 7.0 References.....                               | 24 |

### **Part B: Petrology and Geochemistry of Primitive Achondrite Northwest Africa 11042.....**

|                       |    |
|-----------------------|----|
| Abstract.....         | 28 |
| 1.0 Introduction..... | 28 |
| 2.0 Methods.....      | 29 |
| 3.0 Results.....      | 31 |
| 4.0 Discussion.....   | 34 |
| 5.0 Conclusions.....  | 35 |
| 6.0 Figures.....      | 36 |
| 7.0 References.....   | 48 |

Magmatic Hydrothermal Alteration and Secondary Post-Shock Features in Martian Olivine-  
Phyric Basalt Northwest Africa 10416

Zoltan Vaci et al.

Abstract

The Martian olivine-phyric basalt Northwest Africa (NWA) 10416 contains large olivine xenocrysts whose cores have been stained brown by hydrothermal alteration and whose rims are composed of pristine olivine overgrowths. Microanalysis of these olivine cores reveals various degrees of amorphization, some of which have been overprinted by terrestrial weathering, evident as part of a weathering rind along the exposed surface of the meteorite. Studies of a completely unweathered terrestrial analogue basalt from southern Colorado reveal similar features and indicate that both basalts were altered in a supersolidus magma chamber setting. The alteration features in NWA 10416 thus imply the presence of significant quantities of magmatic water on Mars and a potentially unique igneous reservoir.

1.0 Introduction

The hydrology of Mars has received considerable scientific attention in recent years as evidence mounts for existence of large paleo lakes (1) as well as a currently active hydrologic cycle (2). Since Martian surface geology has largely been shaped by impacts and volcanism, and there is a significant amount of water and CO<sub>2</sub> ice currently present throughout the surface, the existence of impact-driven hydrothermal systems throughout Martian history is a distinct

possibility (3–5). A water-bearing primary magmatic source could also have contributed to Martian hydrologic systems.

Martian meteorites provide a unique opportunity to gather data with a level of precision not possible via orbital or rover analyses. The presence of features such as the multi-phased, cryptocrystalline, and hydrous alteration assemblage iddingsite in the nakhlites provides further evidence for the active role of water in shaping Martian materials. Iddingsite was first characterized in the nakhlite Lafayette as sawtooth-shaped alteration veinlets that cut across pyroxene and olivine grains (6). These contained phyllosilicates and porous oxides. Later work found Ca-siderite along the veinlets' edges and an amorphous silicate gel through their centers (7).

The presence of iddingsite in the nakhlites requires a complex formation and alteration history. Since iddingsite veinlets cut across mineral phases, but not the pristine fusion crust, they were hypothesized to have formed through impact melting of Martian water and CO<sub>2</sub> ice, which created a hydrothermal system (8). Initially, sawtooth cracks formed parallel to the grains' (0 0 1) planes and were widened by dissolution-precipitation reactions which filled them with amorphous Fe-Mg silicate gel. Carbonation reactions then caused the replacement of the gel by siderite, and as the fluid cooled some of the siderite was altered to fibrous smectite clays rimmed by porous oxides and ferrihydrite. The hydrous material in Lafayette was also analyzed by nanoSIMS for its deuterium to hydrogen (D/H) ratio, and the  $\delta D$  of the smectite was found to be elevated by up to ~1400‰ (9). This served to confirm the Martian origin of the hydrous alteration, since Martian atmospheric D/H values are enriched by several thousand permil (10).

The focus of this present study is the hydrous alteration in Martian olivine-phyric basalt NWA 10416. The meteorite has been confirmed as Martian by O isotope analysis (11). It

contains large olivine phenocrysts whose cores have been altered such that they register low oxide totals by electron probe microanalysis (EPMA). The altered cores are surrounded by pristine olivine rims which lack any alteration features. Fractures filled with terrestrial calcite cross-cut these features and are found extensively within the meteorite. The altered cores are not similar to the iddingsite characterized in any previously studied Martian meteorite, however they bear striking resemblance to iddingsite found in some terrestrial basalts. Specifically, they seem to be almost identical to 'iddingsite' as it was initially characterized, as *deuteric* alteration features brought about entirely through magmatism (12). The formation history of this type of iddingsite would eliminate the need to invoke two separate Martian impacts: one to create the hydrothermal system that formed the alteration assemblages and one to loft the meteorite off of the planet's surface. Instead, sub-solidus magmatic alteration would have created the iddingsite before the rock had fully crystallized, after which an impact shocked the stone and eventually brought it into an Earth-crossing orbit.

## 2.0 Methods

Two thin sections each of NWA 10416 and a basalt from La Jara Creek, Colorado, were prepared for analysis by electron probe microanalysis (EPMA) using a JEOL 8200 SuperProbe. One of the thin sections included weathered material near the edge of the stone. Analyses included qualitative energy-dispersive spectroscopy (EDS) and quantitative wavelength-dispersive spectroscopy (WDS), including WDS mapping. An accelerating voltage of 15 kV and a beam current of 20 nA were used for the analyses. Currents were reduced to 10 nA for phases that included volatile elements. Beam spot sizes were generally 1  $\mu\text{m}$ . Standards for major

element chemical analysis were from the Taylor standard block (C.M. Taylor Corp. Sunnyvale, CA).

20×10 μm thin sections were extracted from representative areas in the thin sections and milled to <100 nm thickness using an FEI Quanta 3D Dualbeam field-emission gun (FEG) scanning electron microscope (SEM) focused ion beam (FIB) instrument. Prior to extraction, a 4 μm-thick protective layer of Pt was deposited over the region of interest. Extraction and thinning were performed using a Ga ion beam at an accelerating voltage of 30 kV, while ion beam currents were reduced from 1-3 nA to 0.1 nA by the end of thinning. A final cleaning thinning step of 5 kV and 53 pA was used to clean any material amorphized by the ion beam from the surfaces of the sections. These sections were then analyzed using a JEOL 2010F scanning transmission electron microscope (STEM) operating at an accelerating voltage of 200 kV. Techniques included bright-field and dark-field imaging, STEM imaging, selected area electron diffraction (SAED), and EDS mapping. All analyses were performed in the Electron Microbeam Analysis Facility in the Department of Earth and Planetary Sciences at the University of New Mexico.

### 3.0 Results

#### 3.1 Petrology of NWA 10416

NWA 10416 is an olivine-phyric basalt found in Mali in 2015. The specimen is a single 964 g stone with a desert-varnished exterior that lacks a fusion crust (Fig. 1). Its mineralogy consists of 1-2 mm green-orange olivine phenocrysts (~10 vol%) amidst a groundmass of intragranular pyroxene (~50 vol%) and plagioclase (~30 vol%). Minor phases include ilmenite, chromite, Ti-chromite, titanomagnetite, and Fe-sulfide (13). Pyroxene and olivine grains show

significant compositional variation consistent with magmatic zoning (Fig. 2). Most of the plagioclase is labradoritic (An=63, Ab=36). Approximately 10% of it has been transformed to maskelynite, mostly in contact with or adjacent to shock-melt veins, which are found extensively and cut across all igneous phases (14). The high-pressure phase tissintite was found inside and adjacent to the shock-melt veins (14). Some of the maskelynite has been preferentially replaced by beidellite, a smectite associated with hydrothermal alteration (13).

The most distinct features of NWA 10416 are the large olivine phenocrysts. These are zoned such that the cores are Fo=75, while the rims are Fo=50. The cores are in disequilibrium with the groundmass (Fig. 3), while the rims seem to have equilibrated with a separate population of groundmass olivines. The cores have been stained brown along the edges and orange in the interior due to alteration (Fig. 4A). There are also  $\mu\text{m}$ -sized chromite particles throughout the altered areas. Some olivine cores have been altered further such that their interiors seem to be amorphized, as they appear dark and reflective in optical microscopy (Fig. 4B). The amorphized grains are present adjacent to the exterior of the stone, which has been stained brown by desert weathering. Olivines in the interior of the meteorite do not show this heavy amorphization. Elemental X-ray maps show extensive fractures which have been filled with  $\text{CaCO}_3$ , characteristic of desert weathering. These cut across the alteration features.

Wavelength-dispersive spectroscopic analyses of the altered regions within the olivine phases yield low oxide totals, suggesting the presence of water within the mineral phases. These totals are as low as 65% for some of the heavily amorphized areas.  $\mu\text{X}$ -ray diffraction and Raman spot analysis of dark brown and grey areas in the interior of the alteration have confirmed the presence of Mg-bearing laihunite (15). Terrestrial desert weathering has resulted in extensive

deposition of  $\text{CaCO}_3$  inside of cracks throughout the meteorite. These weathering features cut across the pre-existing olivine alteration (Fig. 5).

### 3.2 Petrology of the La Jara Creek Basalt

The Hinsdale volcanic series is an early Miocene eruptive phase associated with Rio Grande Rift volcanism (16). A basalt sample collected from the west bank of La Jara Creek in southern Colorado shows alteration features similar to NWA 10416 and is thus proposed as a terrestrial analogue for the Martian alteration. Its mineralogy consists of intragranular clinopyroxene, some orthopyroxene, plagioclase, and two populations of olivines. The basalt is also slightly vesicular (3 vol%). Like NWA 10416, the La Jara Creek Basalt (LJCB) contains large (1-2 mm) olivine xenocrysts which are in disequilibrium with the groundmass. The cores are  $\text{Fo}=75$ , while their rims are  $\text{Fo}=50$ . The groundmass contains a second population of smaller olivines which are uniformly  $\text{Fo}=50$  and thus in equilibrium with the xenocryst rims.

The cores of the xenocrysts are stained orange and brown by alteration (Fig. 6), and these altered areas record oxide totals as low as 93% under WDS. LJCB is completely unweathered aside from mild staining <1 mm from exposed surfaces. All olivine xenocrysts show the alteration, regardless of proximity to exposed surfaces.

### 3.3 TEM Microanalysis of Alteration

Three FIB thin sections were extracted from the NWA 10416 olivines: from the interface between the altered olivine core and pristine olivine rim (Fig. 7); from one of the dark brown and grey areas identified as Mg-laihunite (Fig. 8); and from a heavily amorphized area (Fig. 9). The heavily amorphized area is highly porous and contains mostly Fe oxides surrounded by an

amorphous material which also contains low amounts of Al, Ca, and Mg, identified by EDS. The interface between altered core and pristine rim shows an entirely different style of alteration. This region is crystalline olivine, based on electron diffraction patterns, but contains numerous subparallel 10-20 nm wide “tubes” or channels that extend for several hundred nm through the olivine. No additional diffraction maxima are present that would indicate the presence of a secondary alteration phase. Finally, the dark brown and grey areas consist of 200-1000 nm wide diamond-shaped void spaces in linear arrays, rimmed by amorphous material similar in composition and texture to the material found in the heavily amorphized alteration.

An additional FIB section was extracted from LJCB, from the interface between altered olivine core and pristine olivine rim (Fig. 10). The alteration in LJCB olivines is very similar to that found in NWA 10416. Lineations several hundred nm long and tens of nm wide contain amorphized material and some void spaces oriented diagonally to the lineations. Electron diffraction patterns of these regions are consistent with crystalline olivine, but also show the presence of a diffuse ring pattern typical of an amorphous material. This regime appears to be more heavily altered than the alteration found adjacent to the interface between altered and unaltered olivine in NWA 10416, as it contains void spaces. However, it is less extensively altered than the dark brown and grey areas in NWA 10416, since the lineations consisting of amorphous material and void spaces are smaller.

## 4.0 Discussion

### 4.1 Alteration Features

The alteration of the olivine xenocryst cores in both the meteorite and terrestrial samples is unique in that alteration of igneous rocks usually occurs along mineral grain boundaries or the

exteriors of grains. Additionally, ferroan olivines are much more susceptible to oxidation than magnesian ones, so the fact that the forsteritic cores are altered while the fayalitic rims are not suggests that alteration must have occurred before the crystallization of the pristine olivine rims. It is thus extremely unlikely that an entrained xenocryst would become magmatically zoned and then have its cores altered preferentially to its rims.

The presence of terrestrial weathering in NWA 10416 complicates the description of alteration, but the alteration features in the completely unweathered LJCB provide an effectively clarifying analogue. The brown and dark-brown alteration in NWA 10416 must have occurred on Mars before the crystallization of the clear olivine rims, just as it must have occurred in LJCB prior to clear rim formation. The orange heavily amorphized material in the vicinity of the meteorite's weathering rind is a product of desert weathering in which the altered olivine cores were more susceptible to further alteration than the clear rims or the groundmass olivine. This heavy alteration is completely absent in LJCB. Cracks throughout the meteorite have also filled with calcite veins, which is typical of desert meteorite finds. These are ubiquitous and do not show any correlation with the altered cores, except in the case of the orange altered areas adjacent to the weathering rind. Here, EDS maps show a calcite enrichment "halo" around the veins and throughout the heavily altered material, which is further evidence that this heavy alteration is terrestrial.

The Martian alteration could have proceeded due to changing conditions within the magma as it crystallized. In particular, the  $fO_2$  of the groundmass seems to be higher than that of the altered xenocrysts, suggesting that the stability of the xenocrysts was compromised by the surrounding melt. NWA 10426 contains spinels whose compositions range from Ti-poor chromite to Cr-poor titanomagnetite and ilmenite with variable ferric Fe (13). These oxides are

generally associated with the clear olivine rims and groundmass olivine, while none are observed within the altered olivine cores.  $fO_2$  estimates based on chromite, enclosing olivine, and low-Ca pyroxene yield ~QFM-3, while estimates based on Fe-Ti oxides yield ~QFM-1.3±, suggesting that  $fO_2$  increased during crystallization (13).

A similar trend is observed in the terrestrial analogue. LJC B has a single population of spinels which are solid solutions of ulvöspinel and magnetite.  $fO_2$  calculations using the orthopyroxene, olivine cores, and spinels yield ~QFM+2.4 at 1000° C, while calculations using the olivine rims and groundmass olivines yield ~QFM-0.1 at the same temperature and pressure (17). This implies that a higher  $fO_2$  would have been required to maintain equilibrium between the olivine cores and groundmass than between the rims and groundmass, and thus the xenocryst cores likely formed under more reducing conditions than the groundmass and rims. The vesicles in LJC B also imply the exsolution of gases during crystallization. Although there are no vesicles visible in NWA 10426, since the meteorite is heavily shocked their prior existence cannot be ruled out.

Further alteration to the xenocryst cores in NWA 10416 includes the replacement of crystalline olivine by amorphous material, whether in small-scale lineations that include significant voids, or whether through the complete amorphization of large-scale interior areas. O isotope analyses of the xenocrysts reveal that while the clear rims plot in the SNC field, the heavily altered orange areas fall closer to the terrestrial fractionation line (TFL), while the less heavily altered brown areas plot somewhere in between. This is further evidence that the heavily amorphized orange areas are most likely terrestrial weathering features.

All amorphization characterized in this study seems to fall somewhere along a spectrum, beginning with the nanotubes of amorphous material found along the interface of altered and

unaltered olivine in NWA 10416 (Fig. 7), which seems to be the least altered material. The dark brown lineations of void spaces bounded by amorphous material, which are found in the meteorite and LJCB, represent heavier alteration. The void spaces are also clear evidence for fluid dissolution typical of metasomatism of deep crustal or mantle material emplaced in basalt. The completely amorphized material found in the weathered olivines (Fig. 9) are evidence of terrestrial dissolution and replacement.

Clearly, the alteration nanotubes found at the interface must have occurred on Mars since they are bounded by pristine magmatic olivine. The dark brown and grey areas with the large void spaces are found within these cores and are thus also most likely Martian. However, a terrestrial origin is not completely ruled out since they appear to be localized and could have formed from terrestrial water infiltration along cracks. Their similarity to the alteration in LJCB, which is completely unweathered, increases the likelihood of a Martian magmatic origin. The presence of voids in both rocks is evidence of fluid interaction and potentially represent the incorporation of a previously altered mantle or deep crustal material into a magma.

#### 4.2 LJCB Petrographic Systematics

The LJCB terrestrial analogue is useful in that it provides a virtually unlimited supply of destructible sample. This allows for a larger sample size and a discussion of vesicle size distribution and olivine rim growth analysis. Although NWA 10416 does not contain vesicles, if the two alteration regimes are sufficiently analogous, it was most likely volatile components within the magma that altered the xenocrysts. As shock is known to erase secondary features such as vesicles, it is entirely possible that the original rock contained vesicles. LJCB also allows access to a greater number of olivines so that the differences in volumes between

xenocryst cores and pristine rims can be combined with a growth rate model to calculate magmatic residence times.

Volcanologists use the vesicles in pyroclasts and lava flows to document processes of gas exsolution, expansion, and escape. These processes occur during magma ascent due to decompression, and they are controlled by the relative rates of bubble nucleation within the magma. Unfortunately, bubble nucleation in mafic melts is less well understood than in felsic melts and silicic clasts due to a lack of experimental data (18). However, certain patterns hold regardless of vesicularity or chemical composition and can be used to identify nucleation styles and their respective physical constraints. A LJCB thin section area of 18×8.5 mm contains 6,182 vesicles of area greater than 20  $\mu\text{m}^2$ , for a total vesicularity of 3.4%. This is too low for any kinetic modelling, but broad trends can be extracted by comparing the cumulative volume fraction of the vesicles to the logarithms of their areas (Fig. 10) (19). The vesicles are shown to display “ripening”, which is the selective favoring of large vesicles over smaller ones. Ripening occurs because the volatiles in smaller vesicles exert greater outward pressure per unit volume than volatiles in larger vesicles. Pressure minimization of the overall system thus causes larger vesicles to be favored over smaller ones. For this effect to be observed, the vesicles in LJCB had to have formed under some confining pressure, since an open system would have allowed degassing of large vesicles and not shown any ripening.

As a large degree of zoning is present, the olivine cores and rims in LJCB and NWA 10416 must have formed under significantly different conditions. Unlike NWA 10416, there are enough olivine xenocrysts in LJCB for a meaningful rim growth analysis, with the sizes of growth rims as proxies for the time that the cores were entrained in the groundmass before complete crystallization. The areas of 81 xenocryst cores and their rims were measured, and

ellipses were fit around each. Core major axis diameters were subtracted from total grain ellipse diameters to obtain rim thicknesses. Olivine growth rates were assumed to be  $10^{-10}$  m/s, the lower limit of experimental data in a tholeiitic basalt (20). This lower limit was assumed to obtain the maximum residence time for the xenocryst-laden melt in its magma chamber, an average of 7.5 days (Fig. 11). The significant range of rim growth times, from 2 days to over 2 weeks, indicates a turbulent environment capable of mixing “mature” grains with “primitive” ones and erupting and emplacing them simultaneously. Continuous magma recharge is also a possibility.

NWA 10416 does not display primary vesicularity or a statistically significant xenocryst rim population. It also formed on Mars under lower gravity, which allows for deeper magma chambers and fundamentally different crystal settling velocities and ascent rates (21). However, the alteration to which the olivines were subjected to in both regimes is similar enough that LJCB remains a useful analogue.

## 5.0 Conclusions

Before the results of this study, the alteration in NWA 10416 was interpreted as similar to the iddingsite found in nakhlites. The geologic history of the rock would have occurred as follows: (1) formation of the large olivine phenocrysts at depth, (2) emplacement as xenocrysts in a host magma and magmatic zoning, (3) crystallization of the magma, (4) impact which partially melted the basalt shocked some of the plagioclase to maskelynite, (5) creation of a hydrothermal system which altered the olivine xenocrysts to iddingsite and some of the maskelynite to beidellite, (6) an additional impact which lofted the meteorite off of Mars, and (7) terrestrial desert weathering of the surface and along fractures and grain boundaries.

With the evidence from the unweathered terrestrial analogue to NWA 10416, we find that a simpler geological history is more likely to have occurred. This includes (1) formation of the large olivine phenocrysts at depth, (2) emplacement as xenocrysts and alteration by fluids in a host magma with different chemical characteristics than those at which the olivines formed, (3) crystallization of pristine olivine rims over the altered xenocryst cores, (4) impact which shocked some of the plagioclase to maskelynite and lofted the meteorite off of Mars, and (5) desert weathering including the heavy amorphization of the interiors of some olivine cores and the alteration of some of the maskelynite to beidellite. This interpretation would only require a single impact, which seems much more plausible than any multiple impact scenario. Whether the beidellite can form as the result of desert weathering remains to be seen.

## 6.0 Figures



*Figure 1 showing hand sample of NWA 10416. Dark shock melt veins throughout the stone and orange weathering rind along the edges are visible. Olivine phenocrysts are more heavily altered with proximity to weathered areas.*

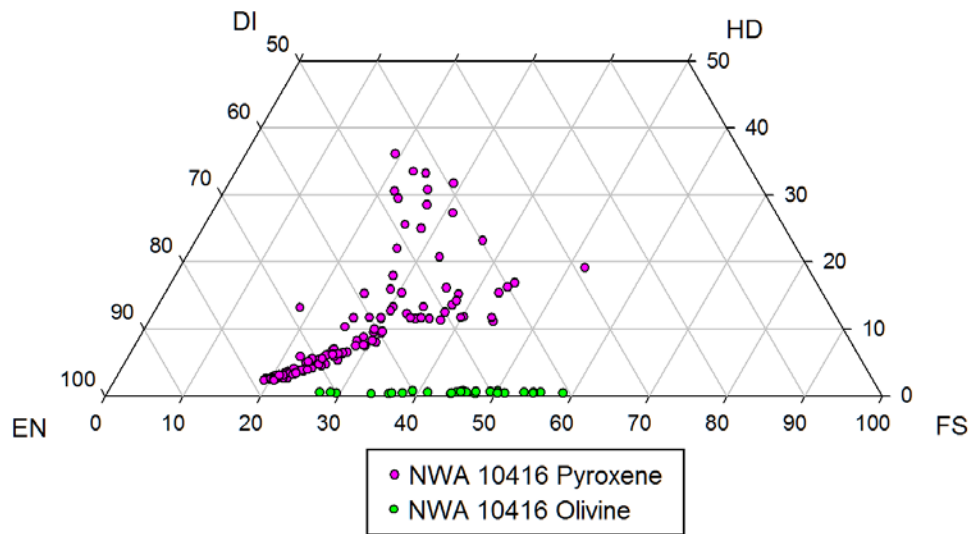


Figure 2 showing pyroxene quadrilateral with NWA 10416 olivines and pyroxenes plotted.

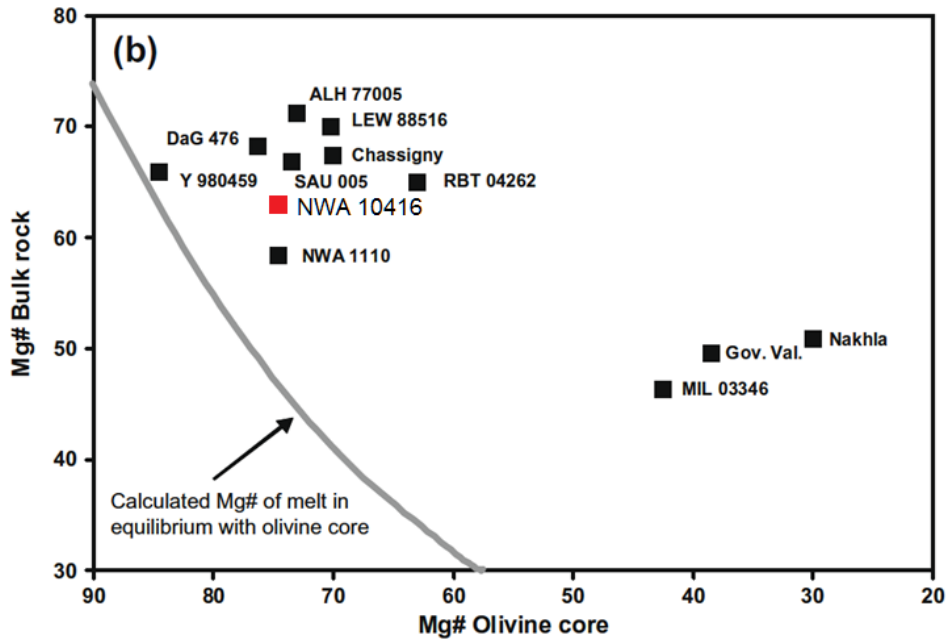
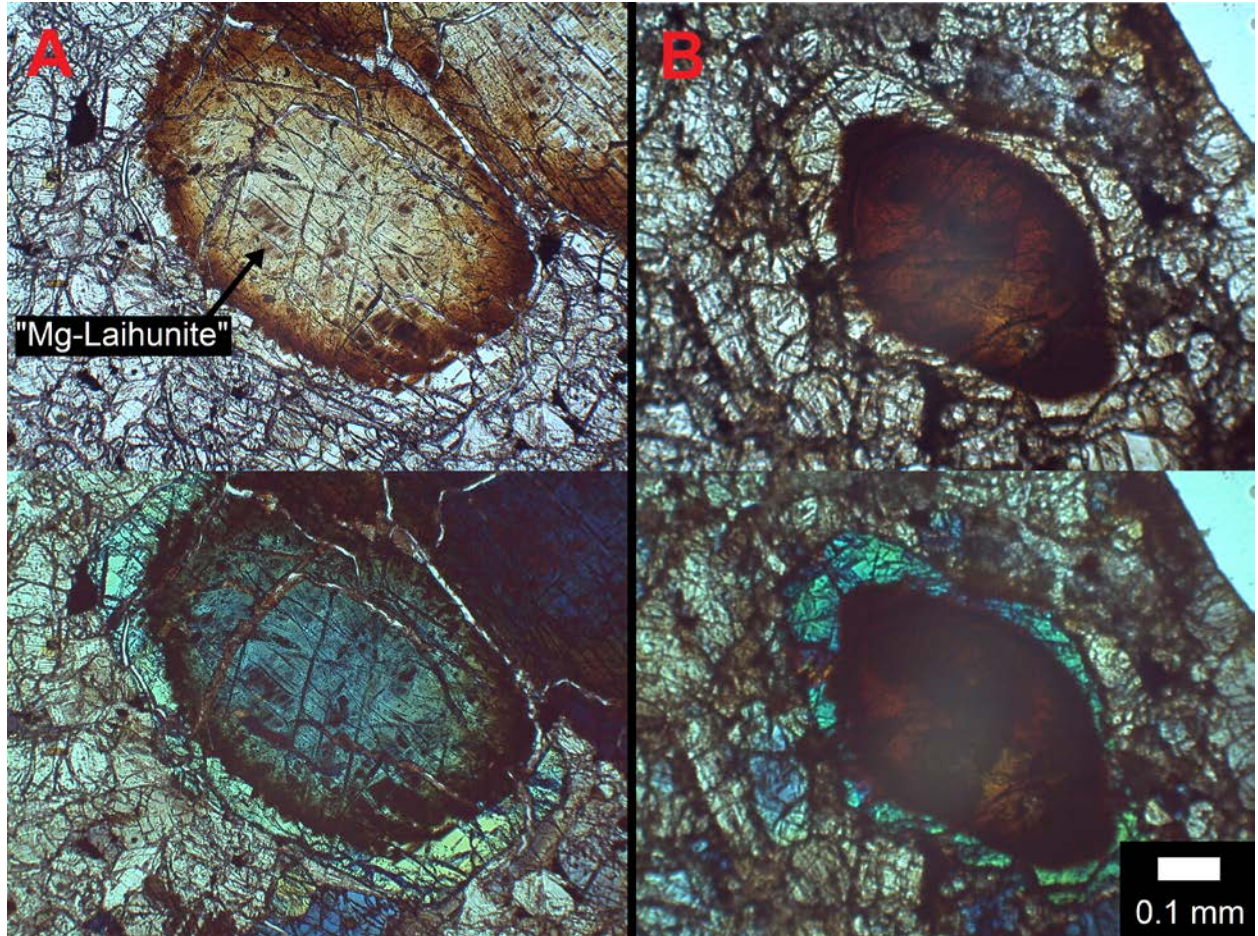
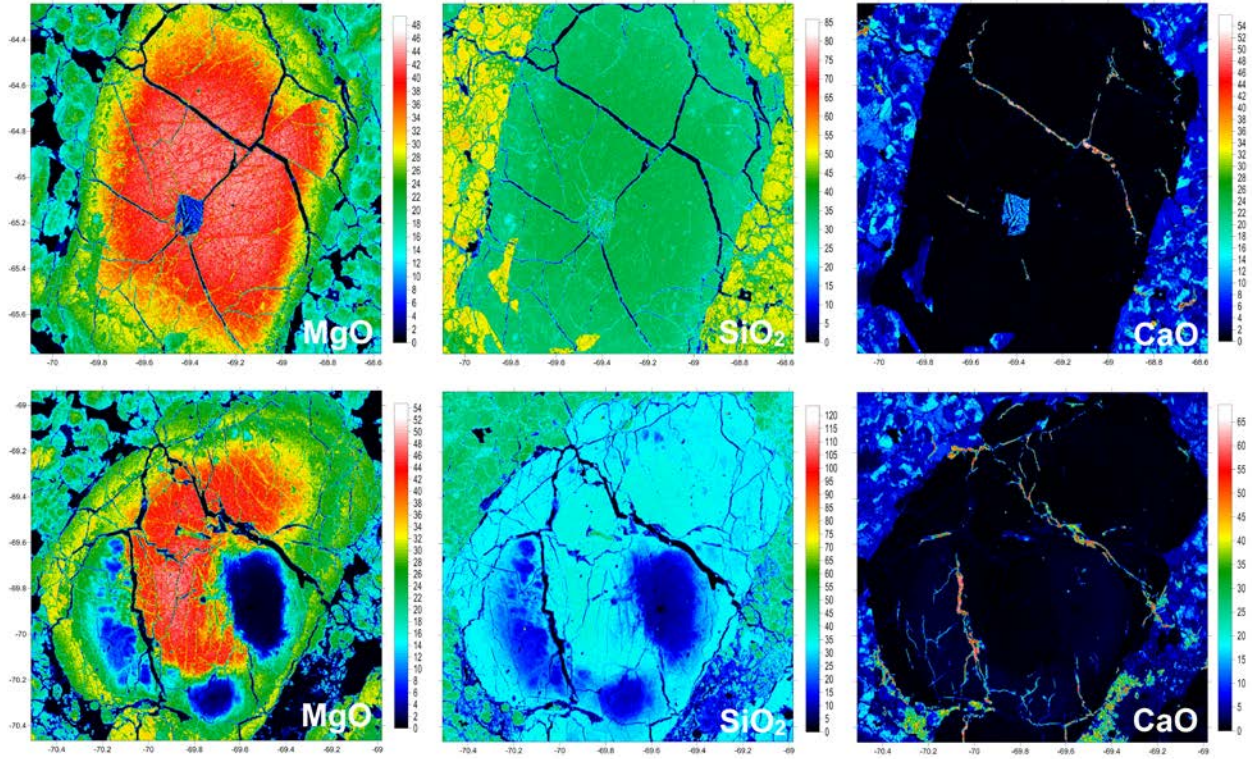


Figure 3 showing bulk rock Mg# [ $Mg/(Mg+Fe)$ ] plotted against the Mg# of zoned olivine cores of various Martian meteorites and NWA 10416. The grey line is a calculated equilibrium curve of the two values. The olivine phenocrysts in NWA 10416 fall off of the curve, indicating that they are xenocrysts. Modified from (22).



**Figure 4** showing plane-polarized light (PPL) (top) and cross-polarized light (XPL) (bottom) optical images of two olivine xenocrysts in NWA 10416. Orange and brown weathered olivine cores are surrounded by pristine olivine rims in crystallographic continuity with the cores and equilibrium with the groundmass. (A) altered olivines display fine lineations of dark brown and grey material identified as Mg-laihunite (15). (B) more heavily altered olivines are darker orange and brown and contain black amorphized areas that are optically opaque.



*Figure 5 showing X-ray quantitative oxide maps of altered olivine grain that corresponds with Fig. 4A (top row) and heavily altered olivine grain that corresponds with Fig. 4B (bottom row). Both are from different areas of the same thin section. Coordinates along the sides of the images are in mm. Oxide percentages are shown in scale bars to the right of each image, with warmer colors corresponding to higher percentages. MgO map shows igneous zoning (top) and heavy depletion in heavily altered areas (bottom). This depletion is paired with Fe enrichment. SiO<sub>2</sub> map shows heavy depletion in heavily altered areas (bottom). CaO maps show terrestrial desert weathering CaCO<sub>3</sub> deposition along cracks. These cracks are surrounded by a blue “halo” in the heavily altered regions (bottom), suggesting that these regions have interacted with terrestrial meteoric water.*

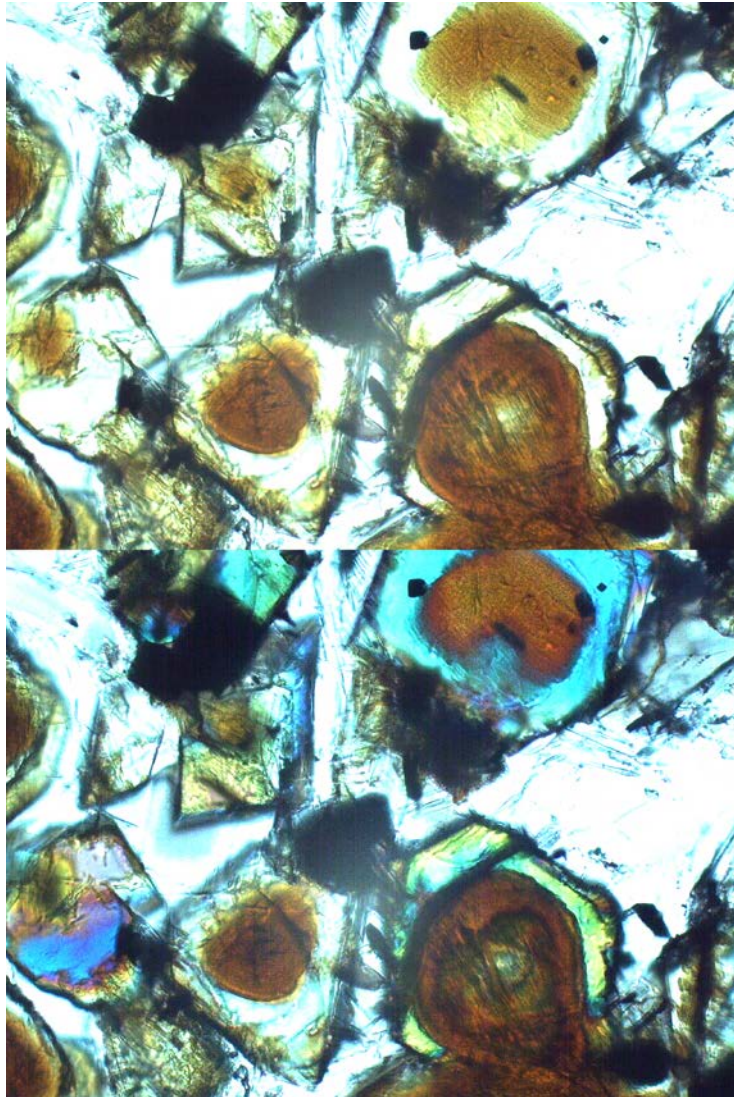


*Figure 6 showing optical PPL image (top) and XPL image (bottom) of altered olivine xenocryst cores surrounded by pristine olivine rims in LJC.*

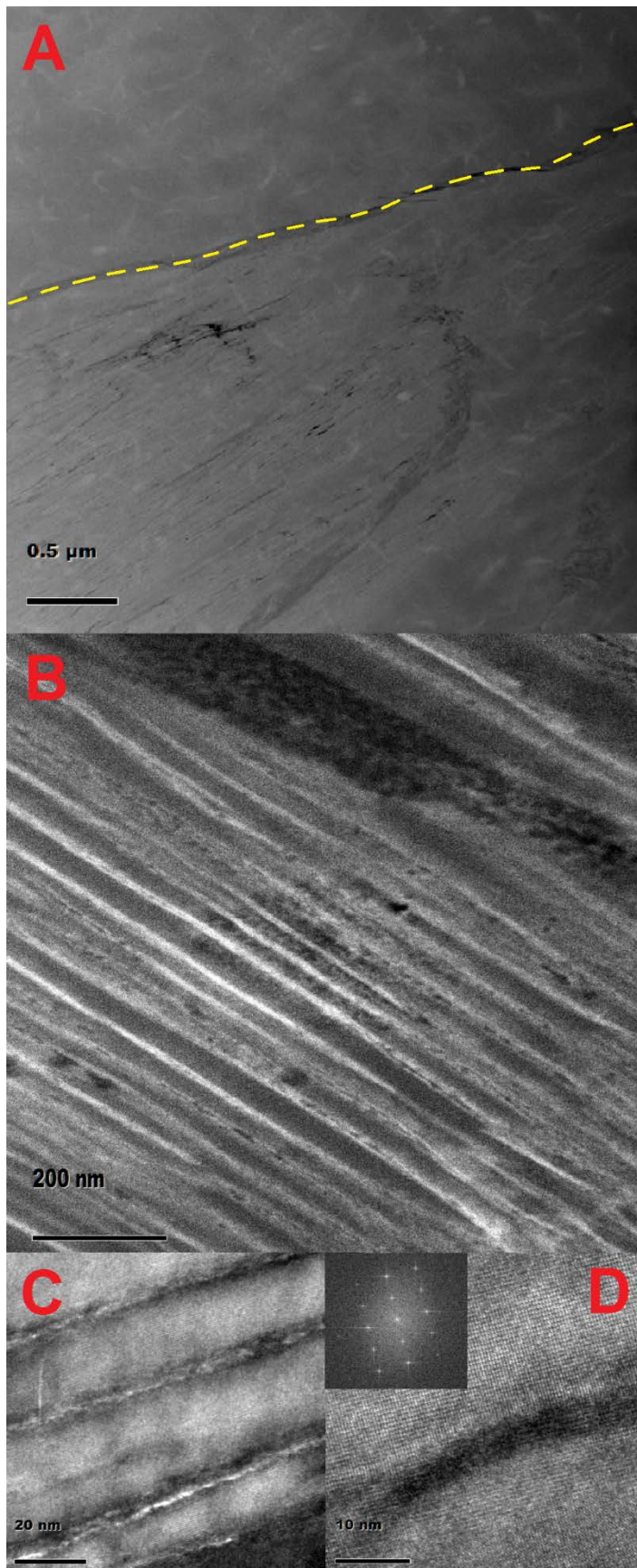


**Figure 7** showing (A) dark-field STEM image of whole FIB section with unaltered olivine rim on the top and altered olivine xenocryst core on the bottom, (B) dark-field STEM image of alteration nanotubes containing amorphous higher Z material than surrounding olivine, (C) high resolution TEM image of nanotubes, and (D) very high resolution TEM image of nanotubes, showing fast-Fourier transform of lattice fringe. The section is parallel to the (210) lattice plane, with the nanotubes lying parallel to the (-120) vector and normal to the [001] axis.

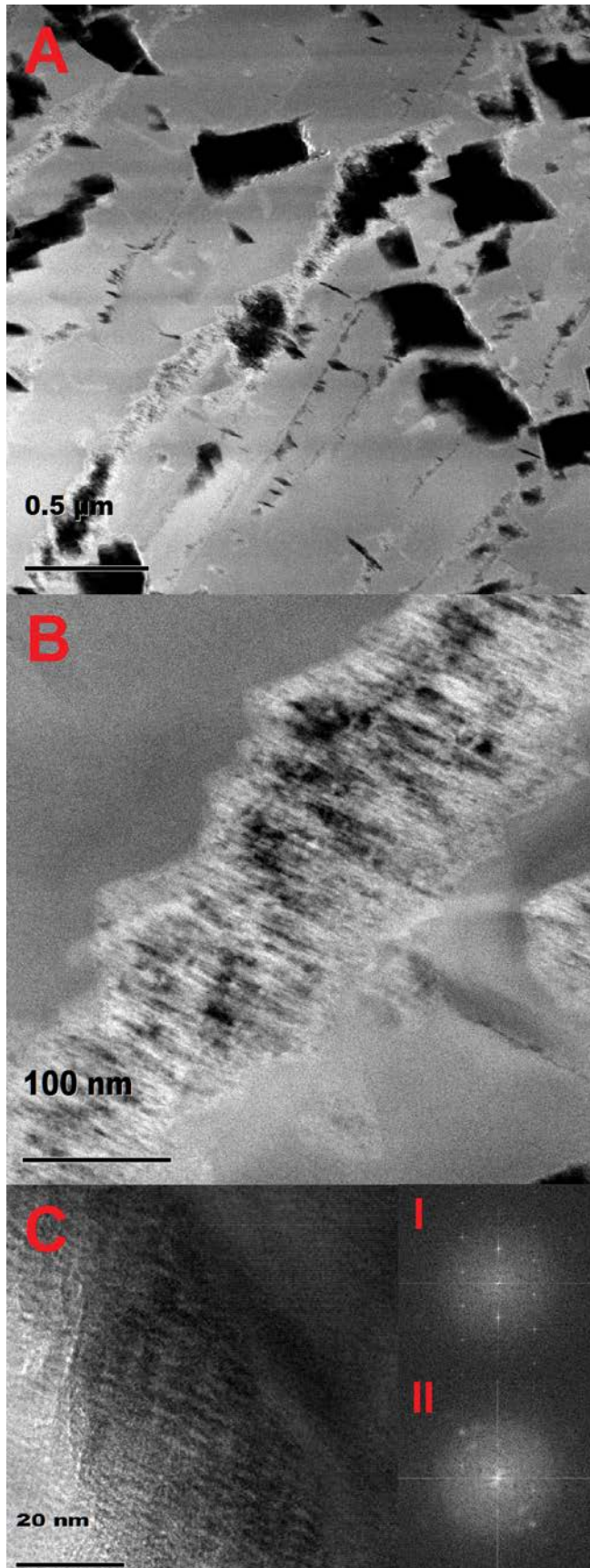


**Figure 8** showing (A) dark-field STEM image of FIB section of dark brown and grey area of altered olivine in NWA 10416, previously identified as Mg-laihunite by  $\mu$ XRD and Raman spectroscopy. The large black areas are voids. (B) dark-field STEM image of amorphized area found in lineations and rimming the voids. (C) high resolution TEM image of amorphous rim (bottom left) adjacent to olivine (top right) and fast-Fourier transforms of olivine lattice fringe (I) and amorphous rim (II).

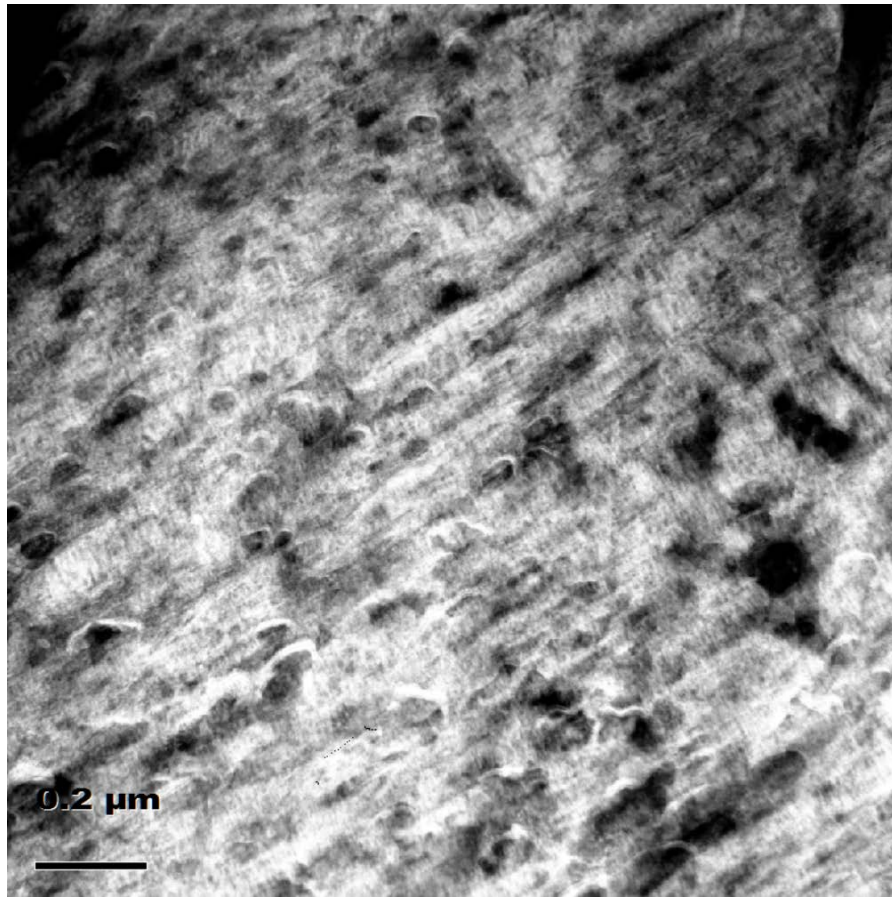


*Figure 9 showing dark-field STEM image of heavily altered olivine xenocryst core from an olivine in a weathered area of NWA 10416 (Fig. 4B). The area is porous and completely amorphized, composed mainly of Fe oxides and minor Si, Mg, and Ca. Lineations in the material are reminiscent of amorphous areas in Fig. 8.*

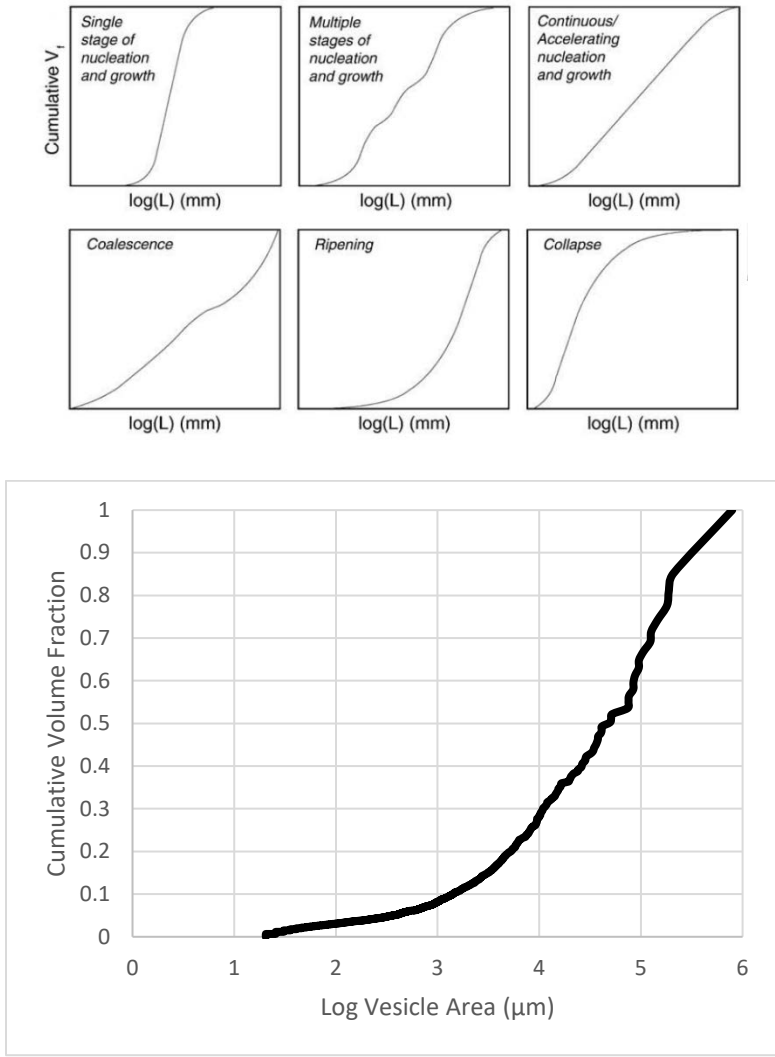


**Figure 10** showing various styles of vesicle size distribution (top) (19) and vesicle size distribution of LJC (bottom). Cumulative volume fraction of vesicles is plotted against the log of each vesicle's area.

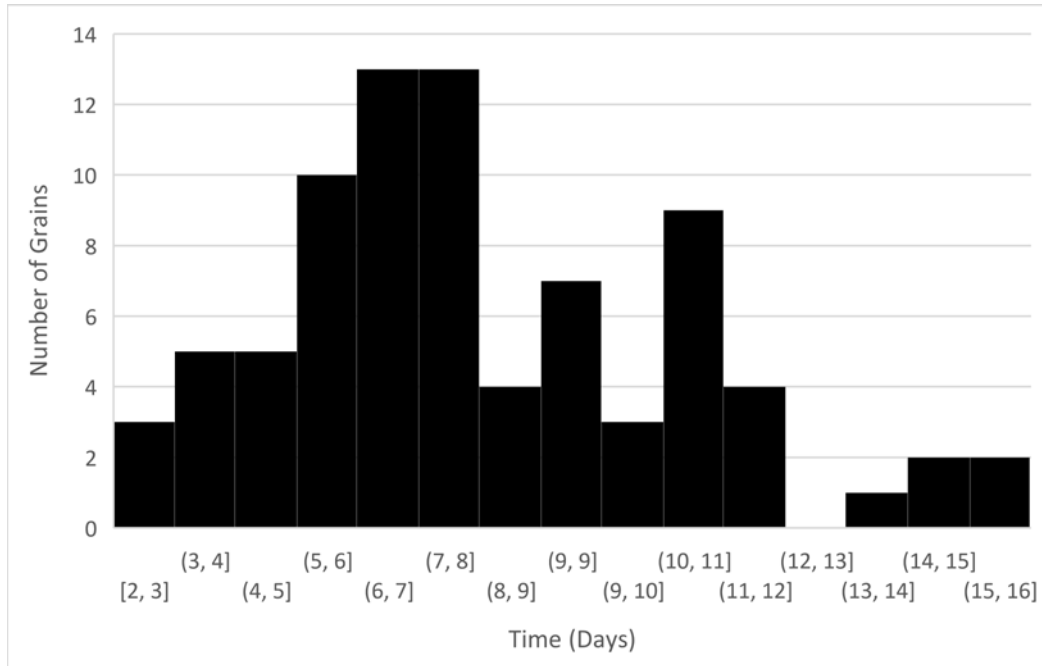


**Figure 11** showing histogram plot of number of days required to grow pristine olivine rims over xenocryst cores in LJC. Average time for the 81 grains measured is 7.5 days.

## 7.0 References

1. J. P. Grotzinger *et al.*, *Science*, in press, doi:10.1126/science.aac7575.
2. C. S. Edwards, S. Piqueux, The water content of recurring slope lineae on Mars, 8912–8919 (2016).
3. D. K. Weiss, J. W. Head, Impact ejecta-induced melting of surface ice deposits on Mars. *Icarus*. **280**, 205–233 (2016).
4. J. P. Cassanelli, J. W. Head, Lava heating and loading of ice sheets on early Mars: Predictions for meltwater generation, groundwater recharge, and resulting landforms. *Icarus*. **271**, 237–264 (2016).
5. J. S. Levy, T. A. Goudge, J. W. Head, C. I. Fassett, Candidate volcanic and impact-induced ice depressions on Mars. *Icarus*. **0**, 1–10 (2016).
6. A. H. Treiman, R. a. Barrett, J. L. Gooding, Preterrestrial aqueous alteration of the Lafayette (SNC) meteorite. *Meteoritics*. **97**, 86–97 (1993).
7. H. G. Changela, J. C. Bridges, Alteration assemblages in the nakhlites: Variation with depth on Mars. *Meteorit. Planet. Sci.* **45**, 1847–1867 (2010).
8. M. R. Lee, T. Tomkinson, L. J. Hallis, D. F. Mark, Formation of iddingsite veins in the martian crust by centripetal replacement of olivine: Evidence from the nakhlite meteorite Lafayette. *Geochim. Cosmochim. Acta*. **154**, 49–65 (2015).
9. T. Tomkinson, M. R. Lee, D. F. Mark, I. A. Franchi, C. L. Smith, in *MetSoc 76* (2013).
10. P. R. Mahaffy *et al.*, The imprint of atmospheric evolution in the D/H of Hesperian clay minerals on Mars. *Science (80-. )*. **347**, 412–414 (2014).

11. K. Ziegler, Z. Vaci, C. B. Agee, Olivines in Martian Meteorite NWA 10416: alteration and oxygen isotope evolution. *MetSoc* 79 (2016).
12. C. S. Ross, E. V. Shannon, The origin, occurrence, composition, and physical properties of the mineral iddingsite. *Proc. U. S. Nat. Mus.* **67**, 1–19 (1925).
13. C. D. K. Herd *et al.*, in *LPSC* (2016).
14. E. L. Walton, O. Tschauner, C. D. K. Herd, C. B. Agee, in *LPSC* 47 (2016).
15. Z. Vaci *et al.*, in *LPSC* (2016).
16. D. P. Miggins, R. A. Thompson, C. L. Pillmore, L. W. Snee, C. R. Stern, Extension and uplift of the northern Rio Grande Rift : Evidence from  $^{40}\text{Ar} / ^{39}\text{Ar}$  geochronology from the Sangre de Cristo Mountains , south-central Colorado and northern New Mexico. *Geol. Soc. Am. Spec. Pap.*, 47–64 (2002).
17. M. S. Ghiorso, B. W. Evans, Thermodynamics of rhombohedral oxide solid solutions and a revision of the Fe-Ti two-oxide geothermometer and oxygen-barometer. *Am. J. Sci.* **308**, 957–1039 (2008).
18. K. V. Cashman, R. Stephen, J. Sparks, How volcanoes work: A 25 year perspective. *Bull. Geol. Soc. Am.* **125**, 664–690 (2013).
19. T. Shea *et al.*, Textural studies of vesicles in volcanic rocks : An integrated methodology (2010), doi:10.1016/j.jvolgeores.2009.12.003.
20. A. Jambon, P. Lussiez, R. Clocchiatti, J. Weisz, J. Hernandez, Olivine growth rate in a tholeiitic basalt: An experimental study of melt inclusion in plagioclase. *Chem. Geol.* **96**, 277–287 (1992).

21. L. Wilson, J. W. Head, Review and Analysis and of Volcanic Eruption To Theory Relationships Landforms. *Rev. Geophys.* **32**, 221–263 (1994).
22. J. J. Papike, J. M. Karner, C. K. Shearer, P. V. Burger, Silicate mineralogy of martian meteorites. *Geochim. Cosmochim. Acta.* **73**, 7443–7485 (2009).
23. A. Ruzicka, G. a. Snyder, L. a. Taylor, Vesta as the howardite, eucrite and diogenite parent body: Implications for the size of a core and for large-scale differentiation. *Meteorit. Planet. Sci.* **32**, 825–840 (1997).
24. H. Yurimoto *et al.*, Origin and Evolution of Oxygen Isotopic Compositions of the Solar System. *Russell J. Bertrand Russell Arch.* **1**, 1–16 (2001).
25. U. W. Bläß, F. Langenhorst, C. McCammon, Microstructural investigations on strongly stained olivines of the chassignite NWA 2737 and implications for its shock history. *Earth Planet. Sci. Lett.* **300**, 255–263 (2010).
26. J. J. Papike, J. M. Karner, C. K. Shearer, Determination of planetary basal parentage: A simple technique using the electron microprobe. *Acta Metal.* **88**, 469–472 (2003).
27. S. Yang *et al.*, Siderophile and chalcophile element abundances in shergottites : Implications for Martian core formation. **24**, 1–24 (2015).
28. W. F. McDonough, S. s. Sun, The composition of the Earth. *Chem. Geol.* **120**, 223–253 (1995).
29. F. E. Jenner, H. S. C. O’Neill, Analysis of 60 elements in 616 ocean floor basaltic glasses. *Geochemistry, Geophys. Geosystems.* **13**, 1–11 (2012).
30. E. Jagoutz *et al.*, in *LPSC X* (1979), pp. 610–612.

31. N. L. Chabot, D. S. Draper, C. B. Agee, Conditions of core formation in the earth: Constraints from Nickel and Cobalt partitioning. *Geochim. Cosmochim. Acta.* **69**, 2141–2151 (2005).
32. A. J. V Riches *et al.*, Petrology and geochemistry of Yamato 984028: A cumulate lherzolitic shergottite with affinities to Y 000027, Y 000047, and Y 000097. *Polar Sci.* **4**, 497–514 (2011).
33. M. Miyahara, E. Ohtani, A. El Goresy, S. Ozawa, P. Gillet, Phase transition processes of olivine in the shocked Martian meteorite Tissint: Clues to origin of ringwoodite-, bridgmanite- and magnesiowustite-bearing assemblages. *Phys. Earth Planet. Inter.* **259**, 18–28 (2016).
34. J. Hu, T. G. Sharp, High-pressure phases in shock-induced melt of the unique highly shocked LL6 chondrite Northwest Africa 757. *Meteorit. Planet. Sci.* **51**, 1353–1369 (2016).
35. D. D. Bogard, D. H. Garrison, M. Norman, E. R. D. Scott, K. Keil, <sup>39</sup>Ar/<sup>40</sup>Ar age and petrology of Chico: Large-scale impact melting on the L chondrite parent body. *Geochim. Cosmochim. Acta.* **59**, 1383–1399 (1995).
36. T. Blackburn, C. M. O'D. Alexander, R. Carlson, L. T. Elkins-Tanton, The accretion and impact history of the ordinary chondrite parent bodies. *Geochim. Cosmochim. Acta.* **200**, 201–217 (2016).

## Petrology and Geochemistry of Primitive Achondrite Northwest Africa 11042

### Abstract

Northwest Africa (NWA) 11042 is a primitive achondrite whose O isotopes plot with the L chondrites, but whose petrology resembles that of a cumulate igneous rock. It is heavily shocked and contains high-pressure phases, indicating an origin on a large parent body that underwent sufficient heating to completely melt it, and experienced an impact large enough to create extensive shock-melt pockets. Microanalysis of these melt pockets, trace element geochemistry, and isochron radiometric dating reveal a possible origin deep within the L chondrite parent body where temperatures were sufficient to produce an igneous rock.

### 1.0 Introduction

Stony meteorites can be broadly grouped into one of two categories. Chondrites are composed of chondrules, agglomerations of primordial dust particles from the solar nebula. Achondrites are composed of material which has been crystallized from a melt and thus does not contain chondrules. Chondrites vary in their degree of aqueous alteration and thermal metamorphism, but all originate from the period of collisional accretion of dust particles in the first ~10 Ma of solar system history. Before the formation of planetesimals and planetary embryos during a period of chaotic growth, all material in the solar system can be said to have been chondritic. Achondrites are chondrites which have undergone magmatic differentiation due to a heating event. Achondritic meteorites originating from the Moon, Mars, and a plethora of small rocky bodies have been recovered and studied extensively. While some of these rocks can be linked to their parent asteroids, such as the Howardite-Eucrite-Diogenite (HED) meteorites

which are thought to originate from the asteroid 4-Vesta (23), many others' origins remain mysteries.

Achondrites' parent bodies are most easily identified by examining their O isotopic composition. By plotting its  $^{17}\text{O}$  against  $^{18}\text{O}$ , relative to standard mean ocean water (SMOW), a meteorite's probable origin is revealed by where it falls on the graph (Fig. 1). Because of fractionation of O in the solar nebula, most planetary bodies have their own O isotopic signature (24). Material from Earth material falls along the terrestrial fractionation line (TFL) which has a slope of 0.52. Lunar material plots very close to this line, the Martian meteorites plot above it in the Shergottite-Nakhlite-Chassignite (SNC) field, and the HED meteorites plot below it in their own field. Primitive achondrites constitute material that lies somewhere between chondrites and achondrites, and this includes groups such as the Acapulcoites, Brachinites, Lodranites, Ureilites, and Winonaites. For example, the Acapulcoites and Lodranites have been melted and partially equilibrated, but they contain relic chondrules. Others have been completely equilibrated but have O isotopes similar to those of certain chondrites.

NWA 11042 (Fig. 2) is a newly discovered achondrite with an anomalous O isotope composition and unique mineralogy, petrology, and geochemistry. Its possible origins and geologic history will be discussed in this study.

## 2.0 Samples and Methods

NWA 11042 was purchased in Morocco in 2016. Two small pieces of NWA 11042 were chipped off the main mass (90.1 g), mounted in epoxy, and polished to 0.05  $\mu\text{m}$  smoothness for microanalysis. Two other pieces were sawed off and made into thin sections. These sections were analyzed by electron probe microanalysis (EPMA) using a JEOL 8200 SuperProbe.

Analyses included qualitative energy-dispersive spectroscopy (EDS) and quantitative wavelength-dispersive spectroscopy (WDS), including WDS mapping. Accelerating voltages were set at 15 kV and electron beam currents were 20 nA. Currents were reduced to 10 nA for phases that included volatile elements. EDS maps were also created using an FEI Quanta 3D field-emission gun (FEG) scanning electron microscope (SEM). Certain areas of these sections were scanned using a Rigaku D/Max Rapid II X-ray diffraction scanner. One of the sections was analyzed for major and trace element geochemistry by laser-ablation inductively couple plasma mass spectrometry (LA-ICP-MS) at Florida State University by Munir Humayun.

1.5 g of material were crushed in a mortar and pestle and sieved to separate 500  $\mu\text{m}$ , 250  $\mu\text{m}$ , 150  $\mu\text{m}$ , and  $\leq 90$   $\mu\text{m}$  sized mineral grains. Care was taken to avoid any weathered material. The  $\leq 90$   $\mu\text{m}$  portion was ground into whole-rock powder, while the other portions were immersed in water and sonicated with a Fisher Sonic Dismembrator Model 300 to remove any impurities from individual grains. These grains were then magnetically and hand-separated into olivine, pyroxene, melt pocket, and maskelynite groups. The olivine, pyroxene, melt pocket, and whole rock groups were used for radiometric dating. Some of the maskelynite and whole rock sample was sent to ETH Zürich for noble gas analysis by Drs. Henner Busemann and Daniela Weimer. The rest of the maskelynite and an additional rock piece was given to Dr. Matt Heizler for Ar-Ar dating at the New Mexico Institute of Mining and Technology. Oxygen isotopes were measured by Dr. Karen Ziegler by laser fluorination at the University of New Mexico.

The olivine, pyroxene, chromite/melt pocket, and whole rock mineral separates were ground into fine powders and dissolved in Teflon bombs with HF and HNO<sub>3</sub> for 72 hours, along with a blank sample. The solutions were then dried down and dissolved in several steps with 6N HCl, 2N HCL, 1N HCl, and finally 1N HNO<sub>3</sub>. A Sm and Nd spike with a known isotopic

composition was also added so that measured isotopic ratios would be normalized to known values. These solutions were then run through two sets of columns to separate out the Sr and rare earth elements (REE). The REE solutions were dried down, dissolved in 0.18N HCl, and run through a different set of columns to separate the Sm and Nd. The Nd and Sr isotopic compositions of these were measured using a Neptune thermal multicollector inductively-coupled plasma mass spectrometer in order to determine their age by Sm-Nd radiometric dating.

### 3.0 Results

#### 3.1 Petrology

NWA 11042 seems to be a cumulate rock whose mineralogy consists of 500-1000  $\mu\text{m}$  anhedral grains of olivine (46 vol%) and pyroxene (38 vol%), smaller grains of maskelynite (15 vol%), chromite (1 vol%), minor troilite and kamacite, and trace taenite and apatite. The olivine is uniform in composition without any signs of magmatic zoning (Fo75). ~95% of the pyroxene is enstatite (En74 Fs20 Wo6), while ~5% is augite (En50 Fs10 Wo40). Any plagioclase that the rock might have had has been shocked to glassy maskelynite which is surrounded by radiating fractures projecting into surrounding olivine or pyroxene grains. Any kamacite or taenite is found paired with the troilite.

The most interesting features in NWA 11042 are the large shock-melt pockets (Fig. 3). These contain high-pressure phases such as ringwoodite, identified optically as large blue grains (Fig. 3) and using X-ray diffraction (Fig. 4). These are accompanied by other unidentified cryptocrystalline phases. Some of the olivines around the pocket have been stained brown due to shock-induced strain such as in the Chassignite NWA 2737 (25). Other olivines show undulatory extinction under cross-polarized light (XPL). All phases present in the meteorite are

represented as partially melted within the shock-melt pockets. Melted areas are enriched in free metal relative to the groundmass. Shock veins are also present in the sample, but the pockets are much more prevalent. In backscattered electron (BSE) images, the melt pockets have dark (low Z) rims which show exsolving metal particles (Fig. 5).

### 3.2 Oxygen Isotope Systematics

NWA 11042 has a  $\Delta^{17}\text{O}$  value of 1.03, which plots it in the domain of the ordinary chondrites on a triple-O diagram (Fig. 6). This places it significantly above the SNC field, although this does not preclude a Martian origin. Other Martian meteorites, such as the polymict breccia NWA 7034, also plot significantly above the SNC field. Within the ordinary chondrites, NWA 11042 plots closest to the L chondrites (Fig. 7). Individual analyses form a trend with a slope of 0.69, which falls in between the slope of the TFL and the carbonaceous chondrite anhydrous mineral (CCAM) line.

### 3.3 Trace Element Geochemistry

LA-ICPMS shows major and trace element geochemistry largely typical of an igneous meteorite. The REE pattern of the bulk rock is almost completely flat and  $\sim 2\times$  CI chondritic (Fig. 8). The maskelynite shows a positive Eu anomaly, while the pyroxenes show complementary negative Eu anomalies. This is characteristic of a reducing magmatic environment in which most of the Eu was incorporated into the plagioclase in a divalent state. The melt pockets show smaller positive Eu anomalies, indicating plagioclase input. Fe/Mn ratios of the olivines are  $\sim 50$ , while the pyroxenes are  $\sim 30$ . These ratios can be used to identify the parent bodies of planetary basalts (26) (Fig. 9). Olivines plot close to Mars and pyroxenes plot

between Mars and Vesta, but there is enough spread in the data for these results to be inconclusive. However, a terrestrial origin is further ruled out.

Major and trace element concentrations for NWA 11042 are shown in Table 1. The meteorite is depleted in volatile elements for an igneous rock. For example, the Ga/Al ratio is lower than that of SNCs and terrestrial rocks by an order of magnitude (27–29) (Fig. 10). Germanium content in pyroxenes is at or below the detection limit, which is about two orders of magnitude below terrestrial and SNC values (30). The abundances of Ni and Co in the olivines are also significant, since these siderophile elements are depleted relative to CI in planetary mantles due to core formation and their metal/silicate partition coefficients scale with temperature in pressure (31).

### 3.4 Sm-Nd Systematics

The  $^{147}\text{Sm}$  and  $^{143}\text{Nd}$  isotopes of the olivine, pyroxene, melt pocket, and whole rock samples were plotted against each other so that the points would form an isochron (Fig. 11) with the linear equation  $^{143}\text{Nd}/^{144}\text{Nd} = ^{143}\text{Nd}/^{144}\text{Nd}_0 + ^{147}\text{Sm}/^{144}\text{Nd} * (e^{\lambda t} - 1)$ , where  $^{143}\text{Nd}/^{144}\text{Nd}_0$  is the initial value at time  $t$ , and  $\lambda$  is the decay constant of the alpha decay of  $^{147}\text{Sm}$  to  $^{143}\text{Nd}$ ,  $6.539 \times 10^{-12}$  /yr. The olivine, pyroxene, and whole rock points form a line with  $t = 4.1 \text{ Ga} \pm 160 \text{ Ma}$ . The melt pocket does not plot on this line, and including it in the isochron gives an age of  $3.4 \pm 3.2 \text{ Ga}$ , which indicates that the melt pocket ages were reset at a much later time than the crystallization age of the rest of the rock.

## 4.0 Discussion

Texturally, NWA 11042 bears significant resemblance to the lherzolitic shergottites, which are Martian cumulate rocks generally composed of olivine, pyroxene, maskelynite, and chromite (32). The level of shock in this meteorite is extreme. The complete absence of crystalline plagioclase, the extensive presence of sub-cm sized shock-melt pockets, and the existence of high-pressure phases within these pockets are all suggestive of an extremely large and violent impact event. This could imply a Martian origin, since large impactors and their associated shock pressures are necessary to loft objects off the Martian surface. The existence of ringwoodite also suggests other high-pressure phases such as bridgmanite and magnesiowüstite might also be present, as in the shock-melt assemblages found in the olivine-phyric shergottite Tissint (33).

The resemblance of NWA 11042 to Martian meteorites ends with its texture. The major element composition, O isotopes, heavy volatile depletion, and flat REE pattern all point to a primitive achondrite with some relationship to the L chondrite parent body. While shock features similar to the ones in NWA 11042 have been identified in ordinary chondrites (34), all of these other samples contain relict chondrules and lack the cumulate textures identified in this meteorite. NWA 11042, meanwhile, is depleted in siderophile elements relative to chondrites, indicating that its parent body probably underwent a differentiation event such as core formation. The only L chondrite that bears some resemblance to NWA 11042 is Chico, which has been interpreted as part of an impact-melt dyke on the L chondrite parent body (35). Chico nevertheless contains relict chondrules and a separate L6 chondrite lithology, but even if NWA 11042 was part of such an assemblage, it would be difficult to explain its large shock-melt pockets which overprint an already magmatically equilibrated groundmass.

The parent bodies of ordinary chondrites have been described as analogous to an onion, with layers increasing in metamorphic gradient with depth (36). Thus the L3 chondrites would have formed the top layer, and the L4-6 layers would have been found progressively deeper. This is recorded in their Pb-Pb ages, which are younger with increasing metamorphism, indicating longer and more intense heating times. As NWA 11042 is the first melt material with L chondritic O isotopes to be studied, a greater depth and thus even younger age within the parent body is expected (Fig. 12). However, an age of ~4.1 Ga is much younger than anything expected to have formed on a small planetesimal such as the L chondrite parent body, whose minimum diameter is thought to be ~260-280 km (36). Therefore, it is more likely that given the extensive and ubiquitous melt pockets throughout this meteorite, the mineral separates were not completely isolated from the melt. This resulted in the younger than expected age.

## 5.0 Conclusions

NWA 11042 is a primitive achondrite whose only real resemblance to ordinary chondrites is its O isotope composition. The petrology and geochemistry of the meteorite suggest an igneous origin on a parent body large enough for complete melting and equilibration to take place. The large shock-melt pockets and high-pressure phases also suggest a large bodied origin, as large impactors are necessary to create the high pressures associated with extensive shock features. A more precise age will be needed before NWA 11042 can be conclusively linked to the interior of the L chondrite parent body, but if dating via Pb-Pb or extinct radionuclides provides a reasonable range, then it will represent the first igneous rock formed on the L chondrite parent body.

6.0 Figures

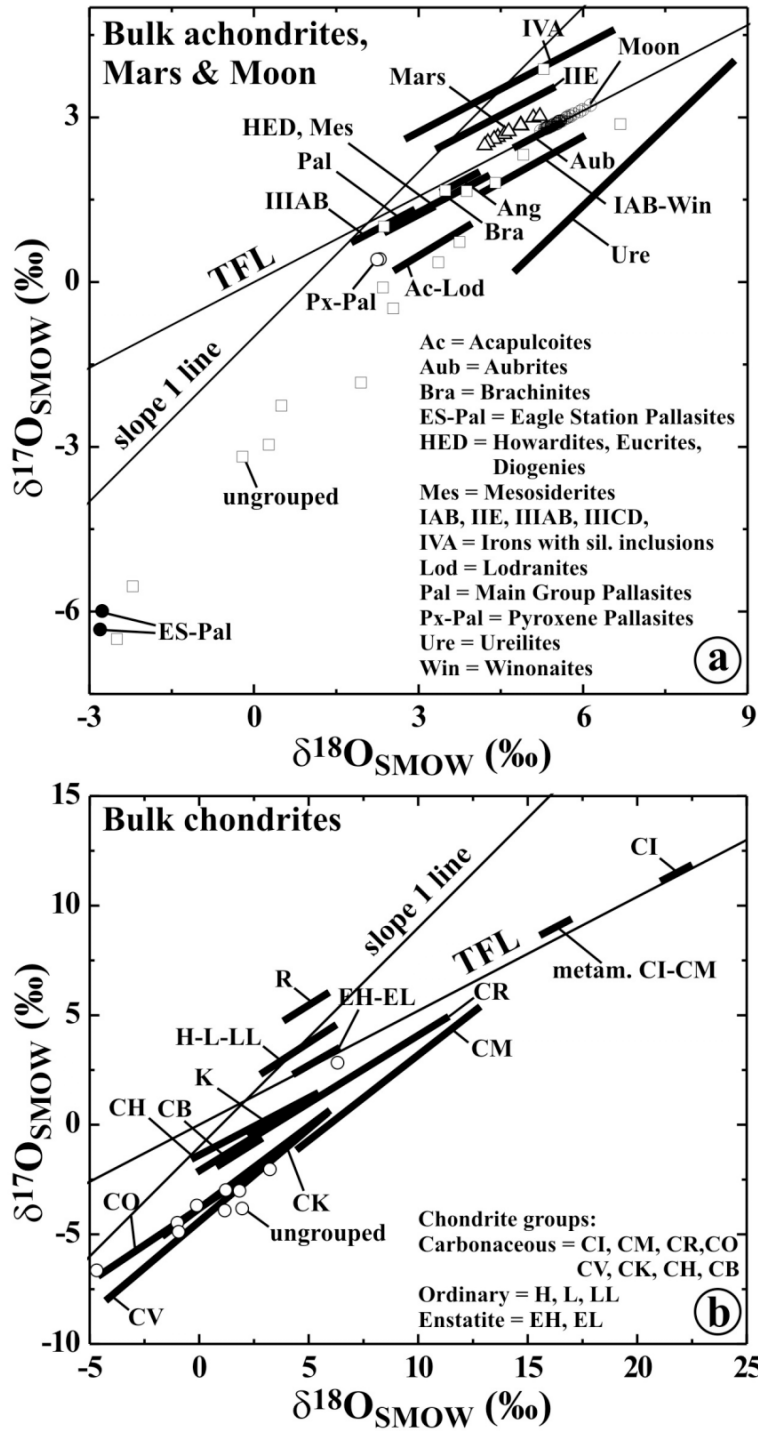
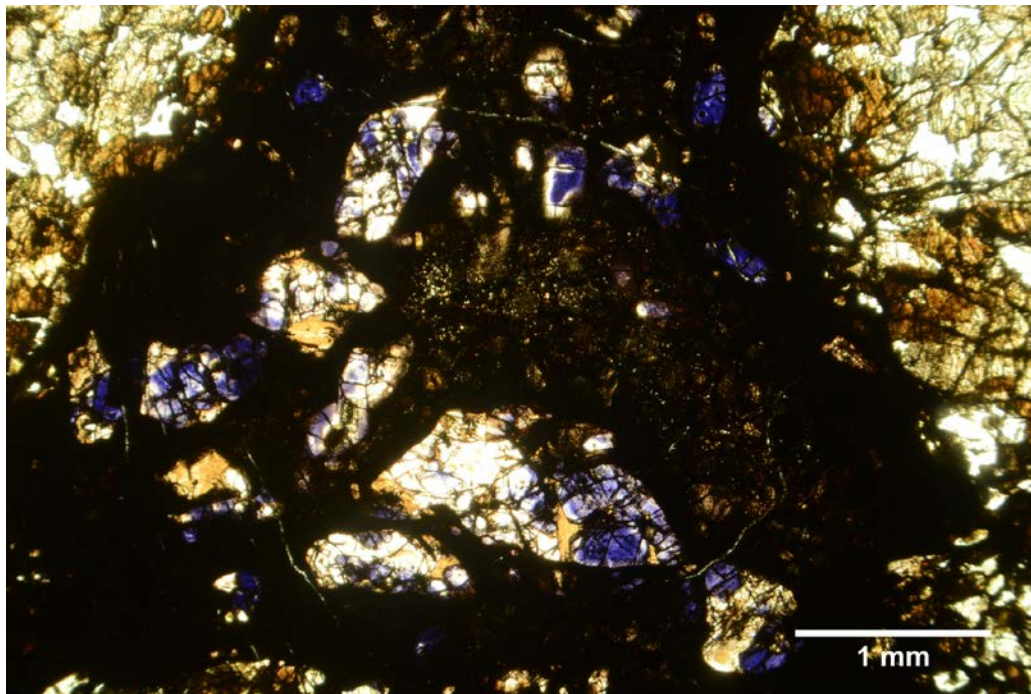


Figure 1 showing O isotope compositions of achondrites (top) and chondrites (bottom). TFL is the terrestrial fractionation line, along which all terrestrial material plots.



*Figure 2 showing hand sample of NWA 11042, found. The presence of a fusion crust indicates that this sample is not very weathered.*



*Figure 3 showing large glassy shock-melt pocket in NWA 11042. Blue grains are ringwoodite.*

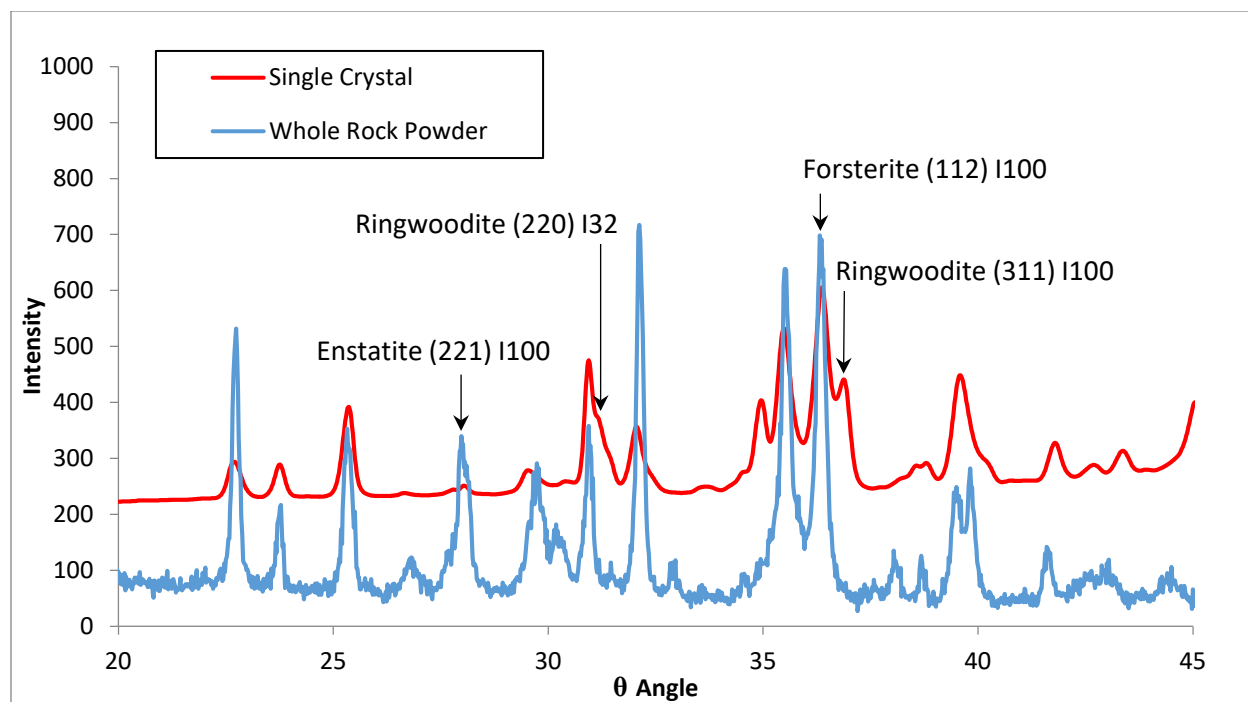


**Figure 4** showing whole-rock powder and single crystal XRD results of a melt pocket in NWA 11042. Bulk mineralogy is mostly olivine (measured as forsterite), pyroxene (measured as enstatite), and maskelynite. The single-crystal beam was focused onto a melt pocket and shows significant characteristic peaks for ringwoodite.

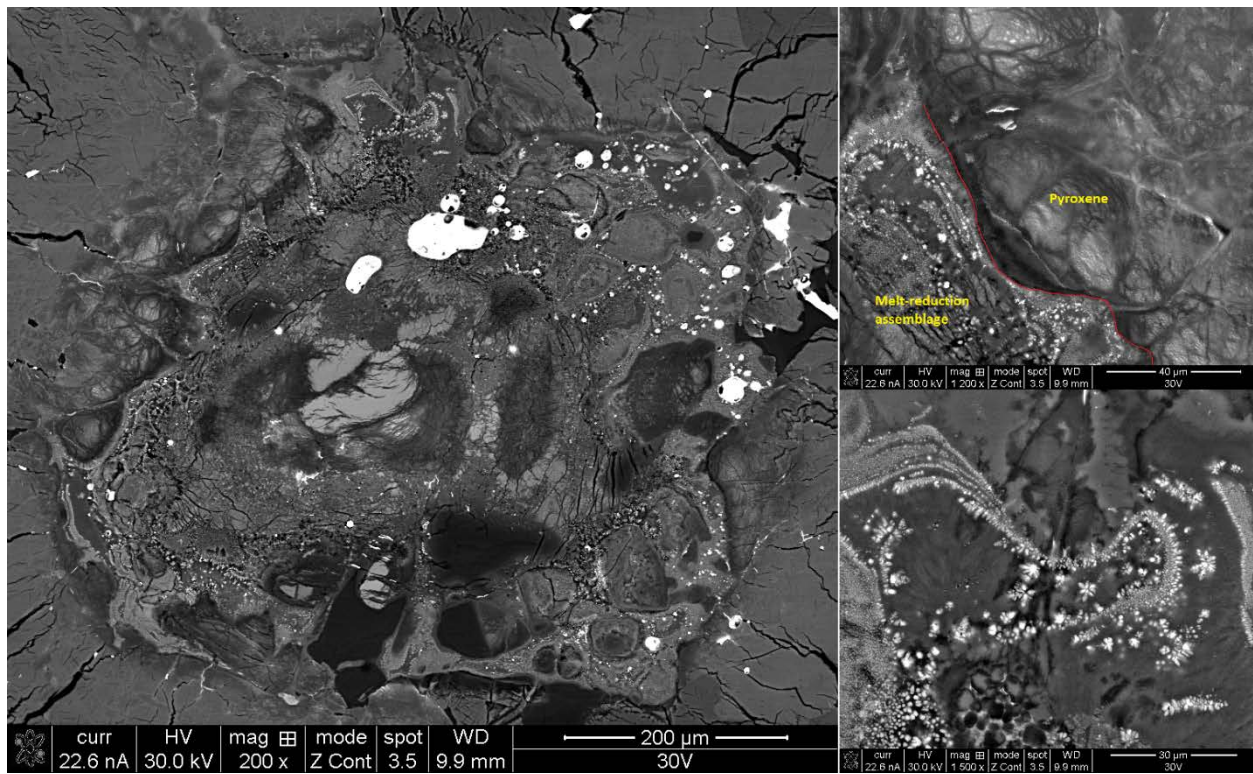


*Figure 5 showing BSE images of a shock-melt pocket in NWA 11042. There is a dark rim around the melt and surrounding grains show exsolving metal nanoparticles (top right). Exsolving metal grains show radiating quench textures (bottom right).*

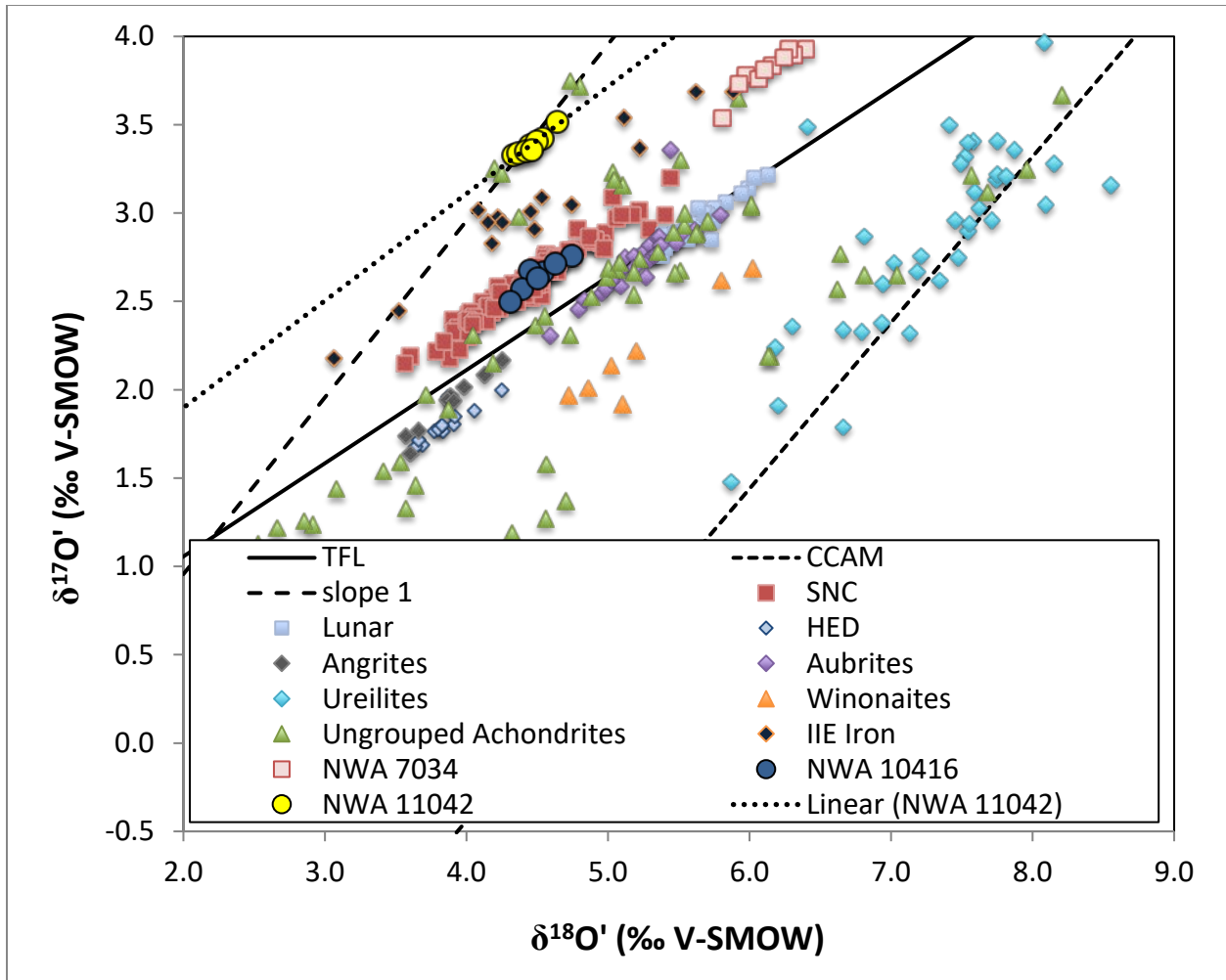


**Figure 6** showing  $\delta^{18}O$  plotted against  $\delta^{17}O$  in ‰ vs. Vienna Standard Mean Ocean Water (V-SMOW) in a triple-O diagram, for NWA 11042, IIE irons, and a variety of achondrites. Also shown are the terrestrial fractionation line (TFL), the carbonaceous chondrite anhydrous mineral (CCAM) line, a linear regression through the NWA 11042 analyses, and a slope of 1 for reference.

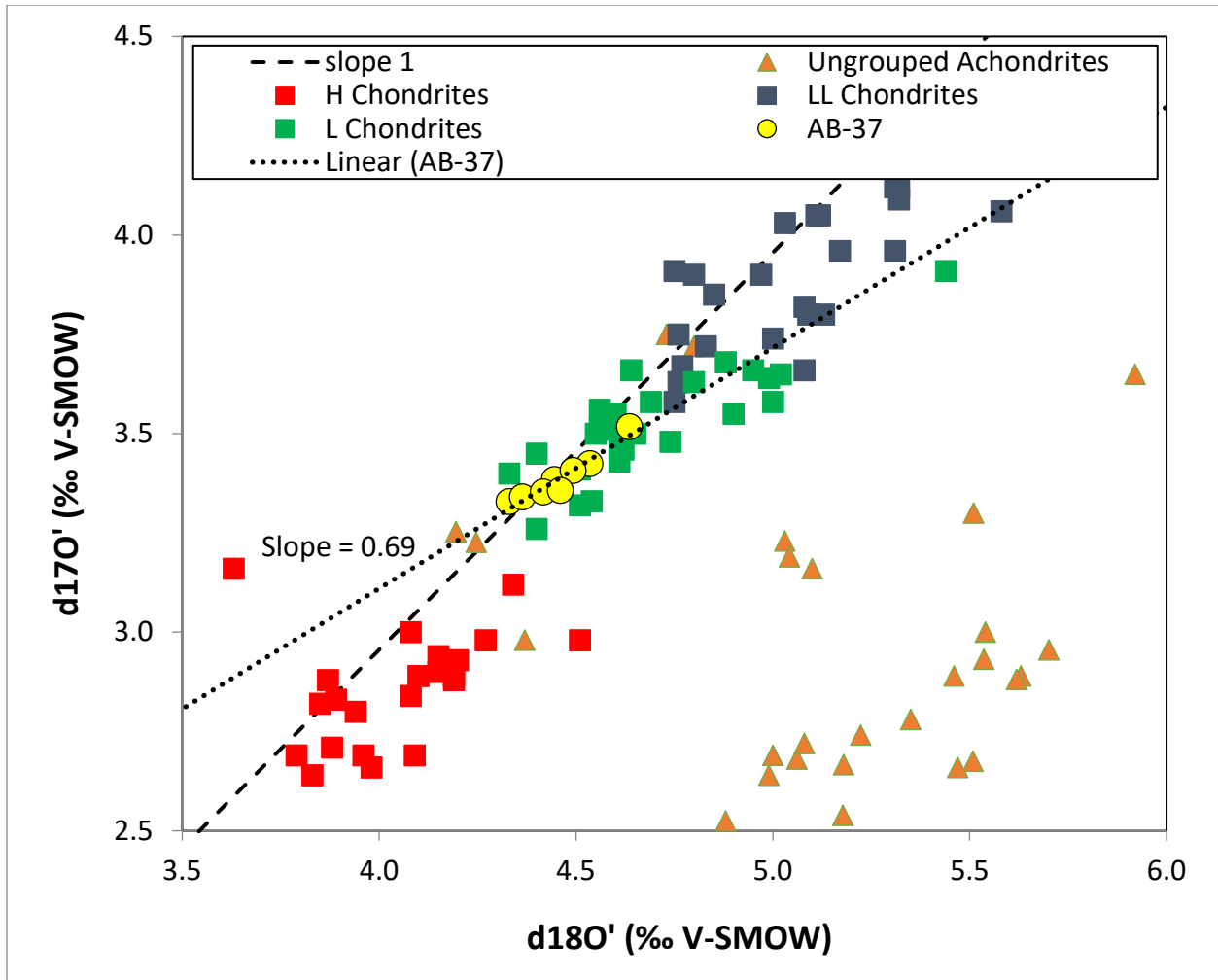


*Figure 7 showing NWA 11042 in triple-O diagram with the ordinary chondrites and some of the ungrouped achondrites. Also shown are a linear regression through the NWA 11042 analyses and a slope of 1 for reference.*

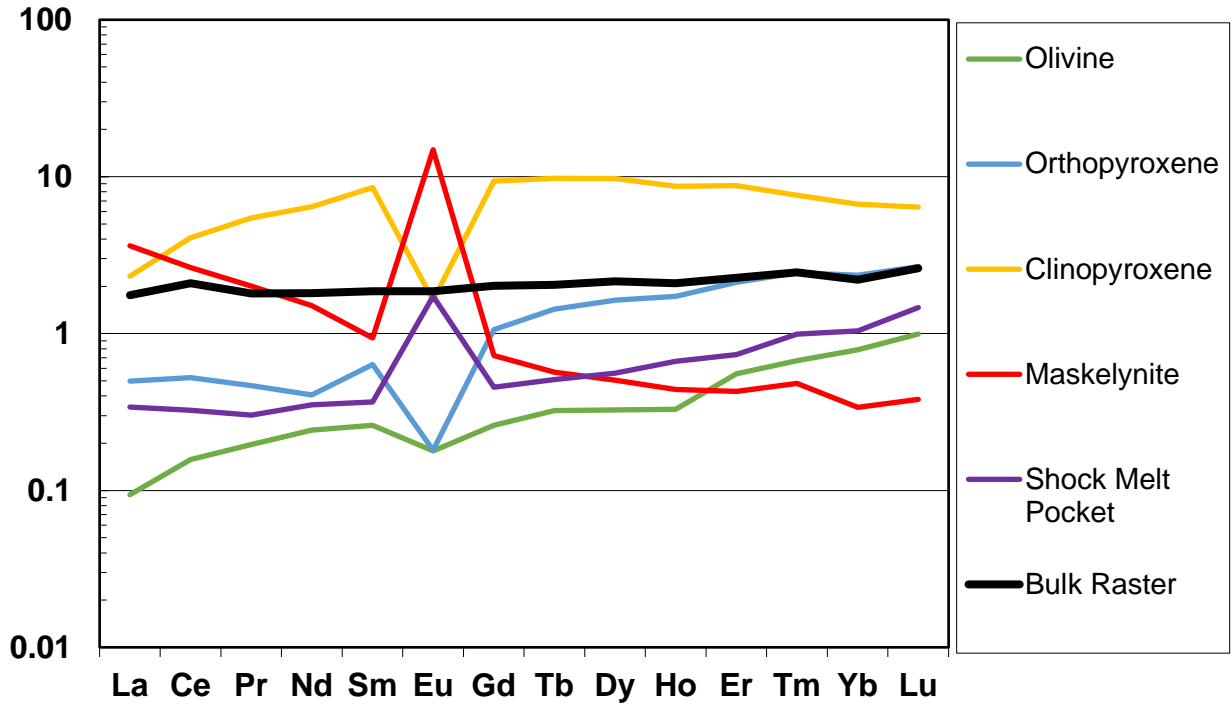


**Figure 8** showing LA-ICPMS measured REE normalized to CI chondrites in the major phases, shock-melt pockets, and a 2×2 mm bulk rock raster of NWA 11042. The maskelynite shows a positive Eu anomaly, while the pyroxenes show a complementary negative anomaly. The shock-melt pockets also contain a Eu anomaly, indicating large amounts of plagioclase input. The positive Eu anomaly in the maskelynite indicates reducing conditions in the magmatic source. Overall, the rock shows an almost flat REE pattern ~2 times higher than chondritic.

|         | Olivine | Opx     | Cpx     | Mask.   | Chromite | Melt    | Bulk   |
|---------|---------|---------|---------|---------|----------|---------|--------|
| n       | 5       | 5       | 3       | 5       | 1        | 6       | 4      |
| SiO2    | 36.85   | 53.49   | 51.30   | 62.19   | 0.15     | 38.31   | 46.52  |
| TiO2    | 0.01    | 0.15    | 0.30    | 0.07    | 3.04     | 0.05    | 0.11   |
| Al2O3   | 0.05    | 0.78    | 1.22    | 20.31   | 9.17     | 2.13    | 2.39   |
| FeOT    | 23.46   | 14.45   | 8.29    | 2.36    | 31.50    | 24.74   | 17.86  |
| MnO     | 0.49    | 0.46    | 0.32    | 0.04    | 0.71     | 0.32    | 0.43   |
| MgO     | 37.99   | 27.14   | 18.78   | 2.19    | 3.34     | 26.38   | 28.60  |
| CaO     | 0.38    | 2.18    | 17.39   | 3.04    | n.d.     | 1.89    | 2.26   |
| Na2O    | 0.55    | 0.42    | 0.67    | 8.31    | 0.57     | 0.81    | 1.02   |
| K2O     | 0.08    | 0.05    | 0.03    | 0.77    | 0.18     | 0.23    | 0.07   |
| P2O5    | 0.02    | 0.03    | 0.02    | 0.12    | 0.00     | 0.04    | 0.08   |
| S       | 0.08    | 0.17    | 0.54    | 0.58    | 0.09     | 4.93    | 0.29   |
| Cr2O3   | 0.05    | 0.69    | 1.13    | 0.01    | 51.33    | 0.17    | 0.35   |
| Total   | 100.00  | 100.00  | 100.00  | 100.00  | 100.07   | 100.00  | 100.00 |
| Mg#     | 74.3    | 77.0    | 80.2    | N/A     | 15.9     | 64.1    | 74.1   |
| FeO/MnO | 48.3    | 31.3    | 25.6    | N/A     | 44.6     | 61.5    | 41.7   |
| K/Rb    | 468     | 329     | 240     | 225     | 148      | 321     | 207    |
| Be      | 0.027   | 0.041   | 0.040   | 0.057   | 0.013    | 0.028   | 0.031  |
| B       | 1.323   | 1.031   | 1.099   | 1.282   | 1.206    | 4.401   | 0.617  |
| V       | 19.758  | 133.420 | 320.117 | 2.139   | 3620.118 | 39.910  | 74.355 |
| Co      | 23.568  | 15.236  | 18.224  | 6.350   | 18.462   | 44.879  | 25.113 |
| Ni      | 54.398  | 21.002  | 128.490 | 35.980  | 33.427   | 312.853 | 91.632 |
| Cu      | 4.828   | 2.737   | 5.487   | 2.625   | 5.770    | 120.519 | 4.890  |
| Zn      | 51.467  | 39.129  | 15.464  | 3.320   | 3000.670 | 67.025  | 45.183 |
| Ga      | 2.489   | 2.578   | 3.052   | 11.382  | 99.540   | 11.640  | 2.565  |
| Ge      | 0.067   | 0.017   | 0.087   | 0.108   | n.d.     | 0.309   | 0.122  |
| As      | 0.407   | 0.047   | 0.060   | 0.043   | 0.060    | 0.839   | 0.058  |
| Rb      | 1.406   | 1.177   | 1.042   | 28.487  | 10.247   | 5.352   | 3.005  |
| Sr      | 6.971   | 2.252   | 10.136  | 111.767 | 1.030    | 65.331  | 13.026 |
| Y       | 0.343   | 2.338   | 11.041  | 0.506   | n.d.     | 0.828   | 2.821  |
| Zr      | 0.711   | 3.213   | 8.845   | 11.074  | 5.318    | 1.396   | 6.336  |
| Nb      | 0.087   | 0.285   | 0.413   | 0.480   | 0.835    | 0.316   | 0.482  |
| Cs      | 0.178   | 0.193   | 0.115   | 0.367   | 0.791    | 0.259   | 0.010  |
| Ba      | 55.610  | 9.655   | 15.469  | 40.327  | 6.654    | 178.338 | 16.435 |
| La      | 0.022   | 0.117   | 0.544   | 0.851   | 0.011    | 0.080   | 0.412  |
| Ce      | 0.095   | 0.316   | 2.460   | 1.587   | 0.023    | 0.196   | 1.262  |
| Pr      | 0.018   | 0.042   | 0.485   | 0.178   | n.d.     | 0.027   | 0.160  |
| Nd      | 0.110   | 0.183   | 2.902   | 0.680   | 0.310    | 0.159   | 0.820  |
| Sm      | 0.038   | 0.093   | 1.253   | 0.138   | n.d.     | 0.054   | 0.274  |
| Eu      | 0.010   | 0.010   | 0.091   | 0.831   | 0.044    | 0.097   | 0.104  |
| Gd      | 0.051   | 0.209   | 1.843   | 0.142   | n.d.     | 0.089   | 0.397  |
| Tb      | 0.012   | 0.052   | 0.354   | 0.021   | 0.003    | 0.018   | 0.074  |
| Dy      | 0.079   | 0.396   | 2.361   | 0.122   | 0.019    | 0.136   | 0.523  |
| Ho      | 0.018   | 0.096   | 0.482   | 0.025   | 0.009    | 0.037   | 0.117  |
| Er      | 0.088   | 0.337   | 1.393   | 0.068   | 0.055    | 0.117   | 0.359  |
| Tm      | 0.016   | 0.059   | 0.184   | 0.012   | 0.023    | 0.024   | 0.059  |
| Yb      | 0.128   | 0.382   | 1.087   | 0.055   | n.d.     | 0.169   | 0.358  |

|              |         |         |         |         |         |         |         |
|--------------|---------|---------|---------|---------|---------|---------|---------|
| <b>Lu</b>    | 0.024   | 0.065   | 0.155   | 0.009   | n.d.    | 0.036   | 0.063   |
| <b>Hf</b>    | 0.025   | 0.087   | 0.297   | 0.324   | 0.138   | 0.040   | 0.216   |
| <b>Ta</b>    | 0.003   | 0.023   | 0.027   | 0.034   | 0.043   | 0.011   | 0.030   |
| <b>W</b>     | 0.005   | 0.005   | 0.018   | 0.011   | 0.010   | 0.012   | 0.061   |
| <b>Re</b>    | n.d.    | 0.000   | 0.000   | n.d.    | 0.012   | 0.001   | 0.006   |
| <b>Os</b>    | 0.017   | 0.001   | 0.001   | 0.001   | n.d.    | 0.006   | 0.006   |
| <b>Ir</b>    | 0.009   | 0.001   | 0.001   | 0.002   | 0.001   | 0.007   | 0.006   |
| <b>Pt</b>    | 0.018   | n.d.    | 0.001   | 0.000   | 0.009   | 0.012   | 0.005   |
| <b>Au</b>    | 0.002   | 0.001   | 0.002   | 0.002   | n.d.    | 0.005   | 0.025   |
| <b>Tl</b>    | 0.007   | 0.002   | 0.005   | 0.001   | 0.009   | 0.178   | 0.013   |
| <b>Pb</b>    | 0.044   | 0.036   | 0.039   | 0.033   | 0.080   | 0.092   | 0.092   |
| <b>Bi</b>    | 0.000   | 0.001   | 0.000   | 0.002   | n.d.    | 0.001   | 0.010   |
| <b>Th</b>    | 0.004   | 0.039   | 0.048   | 0.083   | n.d.    | 0.016   | 0.063   |
| <b>U</b>     | 0.040   | 0.019   | 0.028   | 0.034   | 0.018   | 0.215   | 0.038   |
| <b>Nb/Ta</b> | 28.77   | 12.44   | 15.31   | 14.16   | 19.22   | 29.71   | 16.05   |
| <b>Zr/Hf</b> | 28.03   | 36.85   | 29.81   | 34.17   | 38.51   | 34.68   | 29.30   |
| <b>Th/U</b>  | 0.09    | 2.07    | 1.70    | 2.41    | n.d.    | 0.08    | 1.64    |
| <b>Ni/Ge</b> | 809     | 1215    | 1473    | 332     | n.d.    | 1011    | 748     |
| <b>Ga/Al</b> | 0.01037 | 0.00063 | 0.00047 | 0.00011 | 0.00205 | 0.00103 | 0.00020 |
| <b>Ge/Si</b> | 3.90E-7 | 6.91E-8 | 3.64E-7 | 3.72E-7 | n.d.    | 1.73E-6 | 5.63E-7 |

*Table 1 showing major phases, melt pockets, and bulk raster major element composition in wt% and trace element composition in ppm. n.d. = non-detect; N/A = not applicable.*

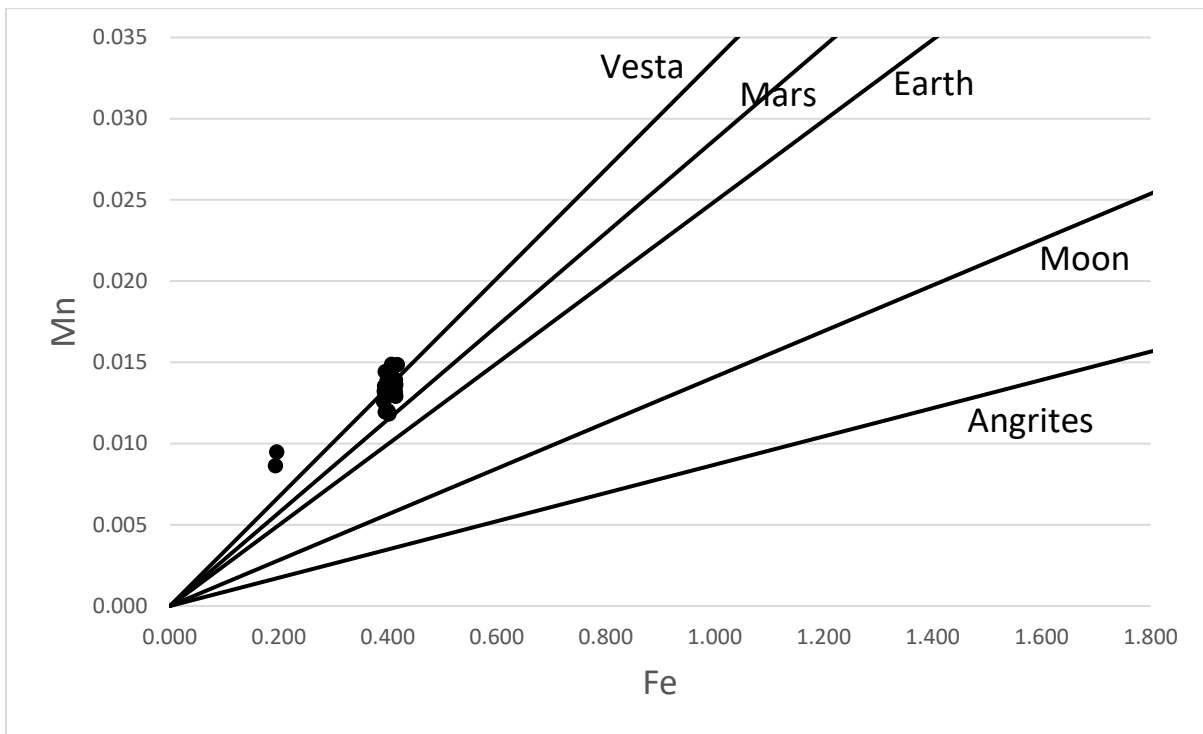
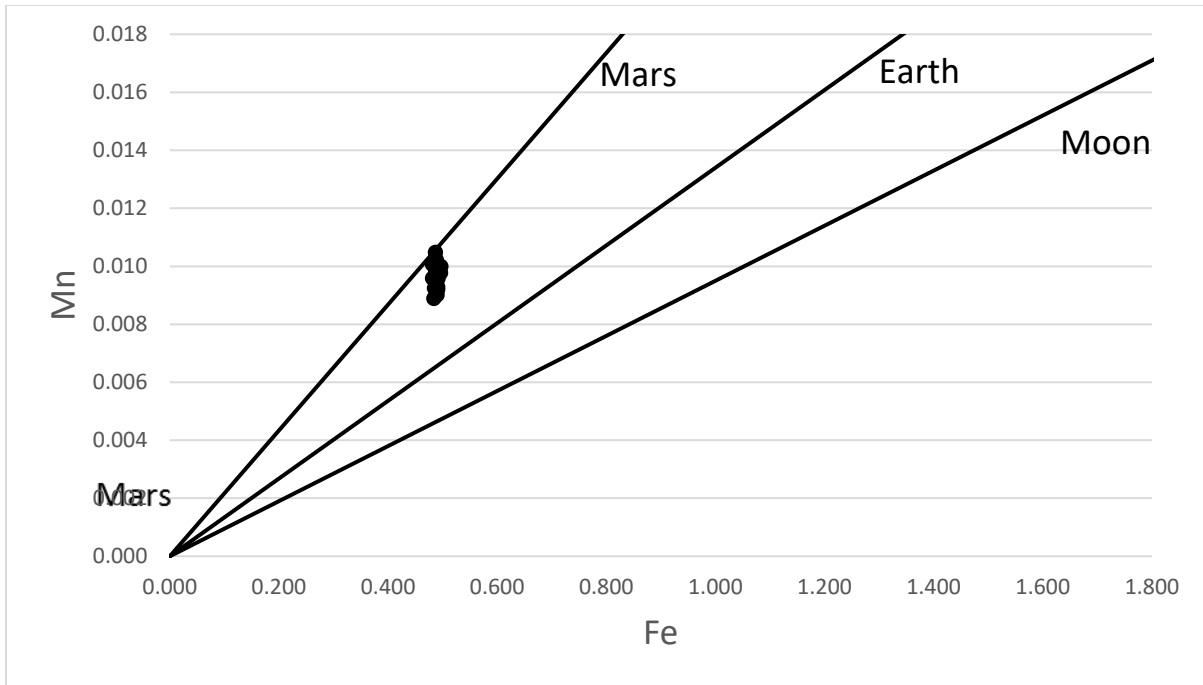


**Figure 9** showing formula ratios of Mn plotted against Fe in NWA 11042 olivines (top) and pyroxenes (bottom), along with the slopes of samples from Earth, the moon, Mars, Vesta, and Angrites. Planetary slopes taken from (26).

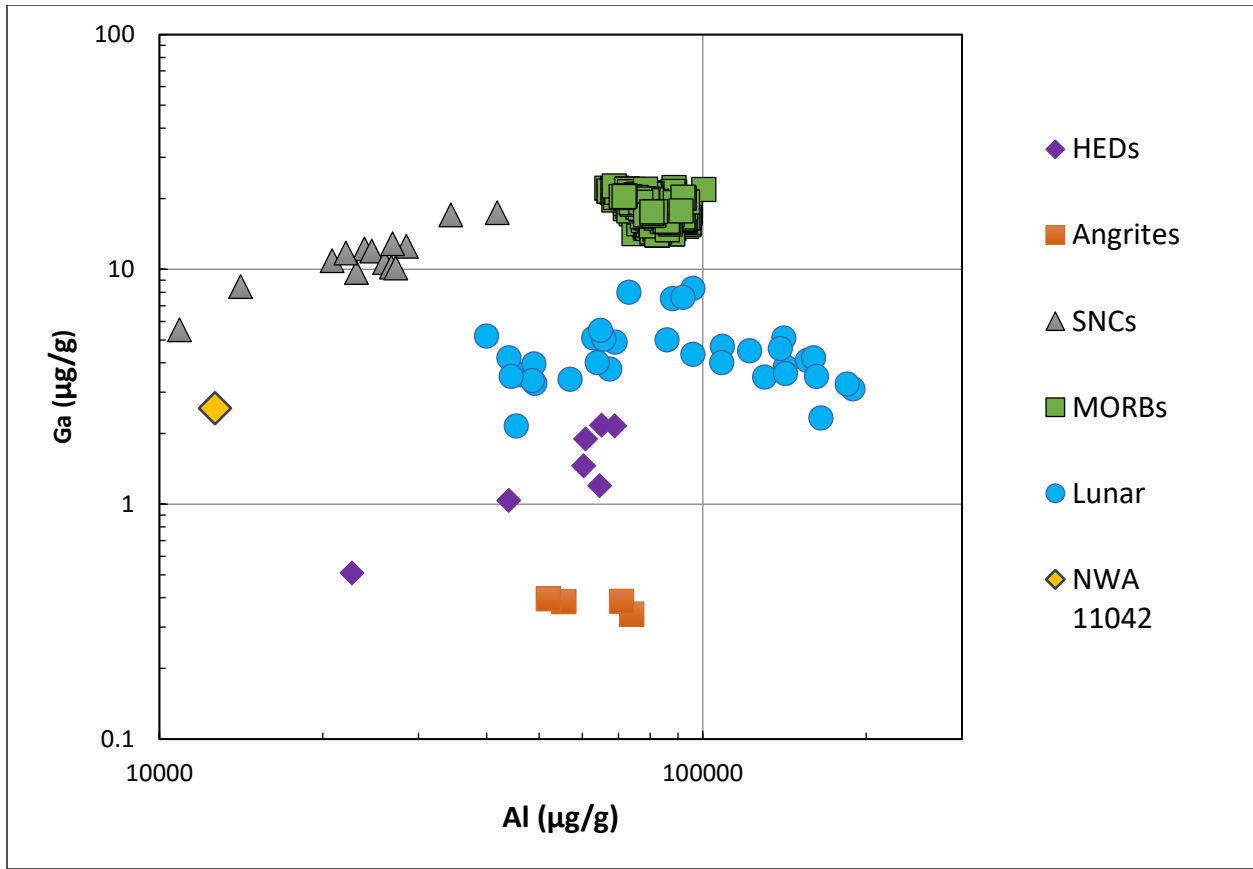


*Figure 10 showing Ga vs. Al content in NWA 11042 and various other solar system material. NWA 11042 is depleted in Ga relative to terrestrial rocks and SNCs.*

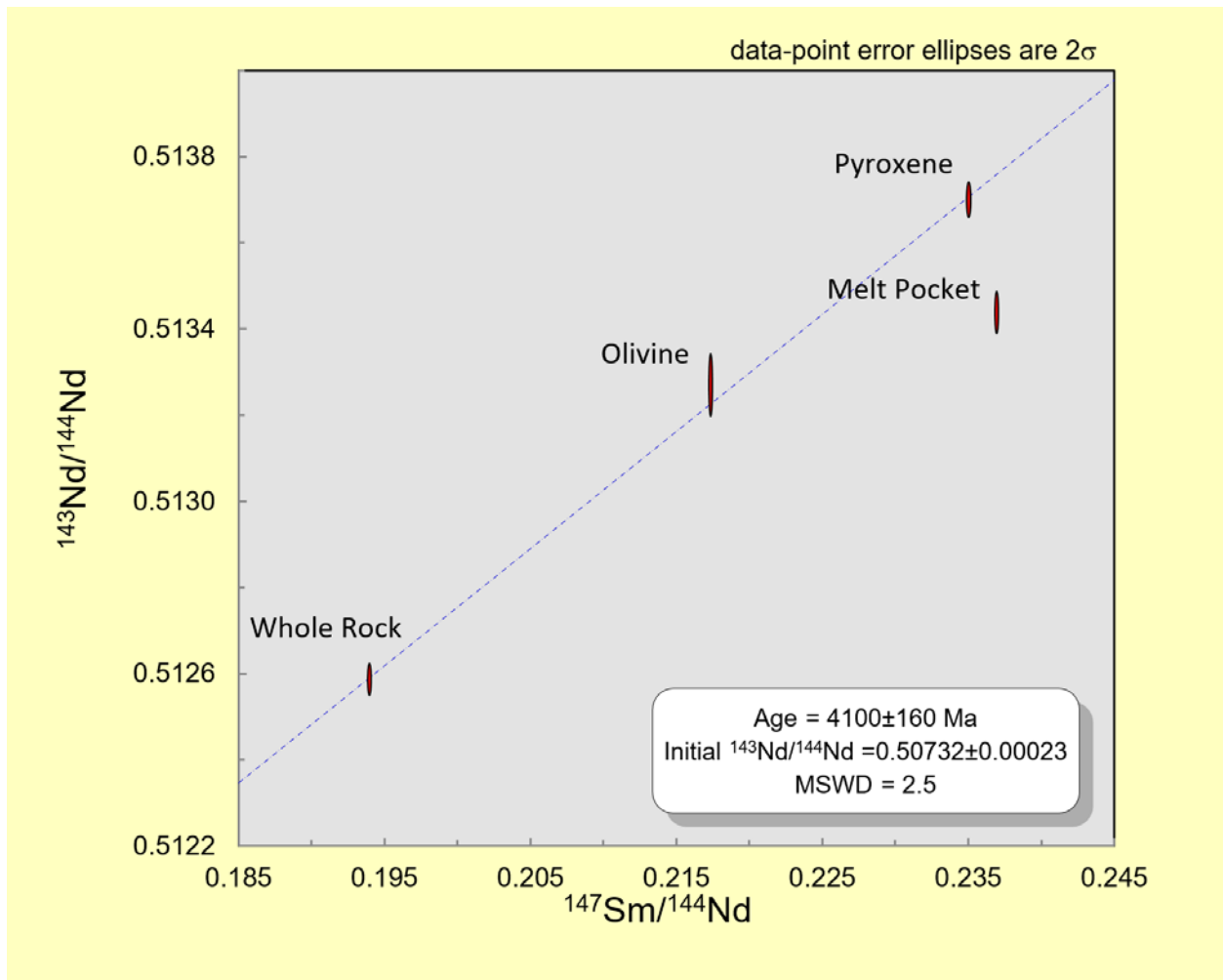


**Figure 11** showing Sm-Nd Isochron for NWA 11042 mineral separates. The age was calculated using olivine, pyroxene, and whole rock data. The melt pocket falls off of the isochron and is much younger than the groundmass.

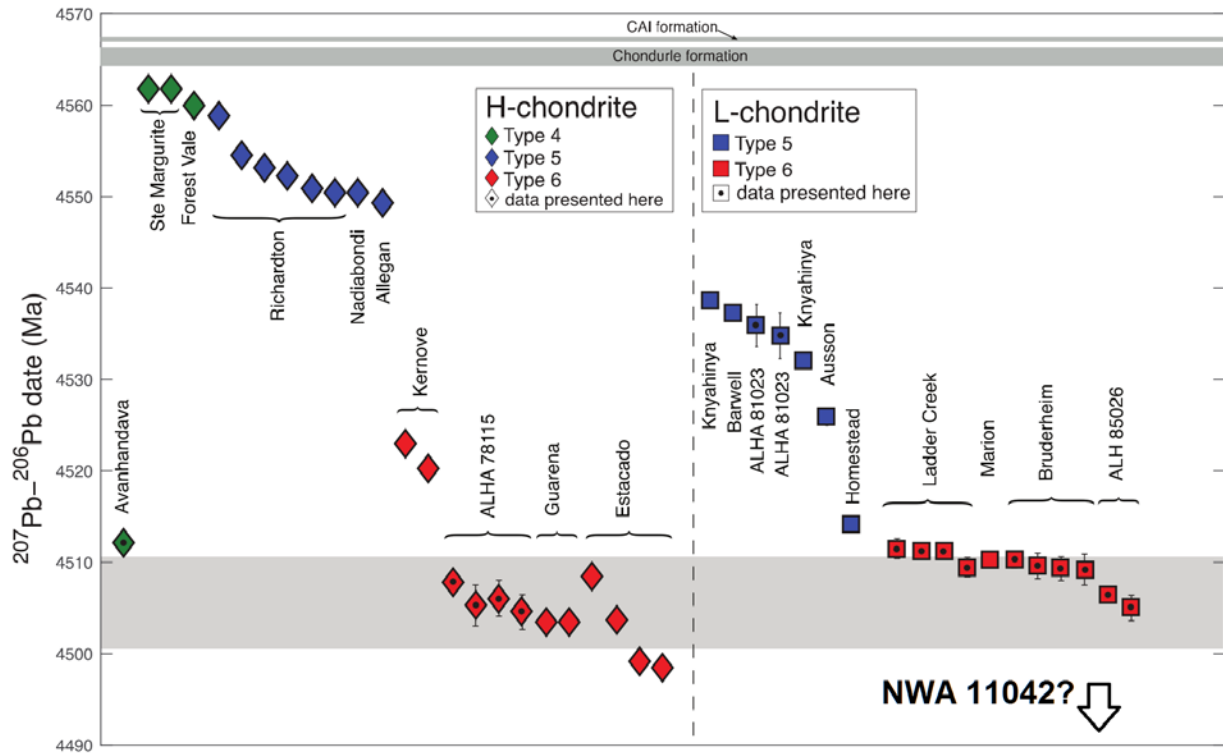


**Figure 12** showing Pb-Pb ages of H and L chondrites, from (36). NWA 11042 is expected to be younger than the L6 chondrites, but Sm-Nd dating is not precise enough to place it on this diagram.

## 7.0 References

1. J. P. Grotzinger *et al.*, *Science*, in press, doi:10.1126/science.aac7575.
2. C. S. Edwards, S. Piqueux, The water content of recurring slope lineae on Mars, 8912–8919 (2016).
3. D. K. Weiss, J. W. Head, Impact ejecta-induced melting of surface ice deposits on Mars. *Icarus*. **280**, 205–233 (2016).
4. J. P. Cassanelli, J. W. Head, Lava heating and loading of ice sheets on early Mars: Predictions for meltwater generation, groundwater recharge, and resulting landforms. *Icarus*. **271**, 237–264 (2016).
5. J. S. Levy, T. A. Goudge, J. W. Head, C. I. Fassett, Candidate volcanic and impact-induced ice depressions on Mars. *Icarus*. **0**, 1–10 (2016).
6. A. H. Treiman, R. a. Barrett, J. L. Gooding, Preterrestrial aqueous alteration of the Lafayette (SNC) meteorite. *Meteoritics*. **97**, 86–97 (1993).
7. H. G. Changela, J. C. Bridges, Alteration assemblages in the nakhlites: Variation with depth on Mars. *Meteorit. Planet. Sci.* **45**, 1847–1867 (2010).
8. M. R. Lee, T. Tomkinson, L. J. Hallis, D. F. Mark, Formation of iddingsite veins in the martian crust by centripetal replacement of olivine: Evidence from the nakhlite meteorite Lafayette. *Geochim. Cosmochim. Acta*. **154**, 49–65 (2015).
9. T. Tomkinson, M. R. Lee, D. F. Mark, I. A. Franchi, C. L. Smith, in *MetSoc 76* (2013).
10. P. R. Mahaffy *et al.*, The imprint of atmospheric evolution in the D/H of Hesperian clay minerals on Mars. *Science (80-. )*. **347**, 412–414 (2014).

11. K. Ziegler, Z. Vaci, C. B. Agee, Olivines in Martian Meteorite NWA 10416: alteration and oxygen isotope evolution. *MetSoc* 79 (2016).
12. C. S. Ross, E. V. Shannon, The origin, occurrence, composition, and physical properties of the mineral iddingsite. *Proc. U. S. Nat. Mus.* **67**, 1–19 (1925).
13. C. D. K. Herd *et al.*, in *LPSC* (2016).
14. E. L. Walton, O. Tschauner, C. D. K. Herd, C. B. Agee, in *LPSC* 47 (2016).
15. Z. Vaci *et al.*, in *LPSC* (2016).
16. D. P. Miggins, R. A. Thompson, C. L. Pillmore, L. W. Snee, C. R. Stern, Extension and uplift of the northern Rio Grande Rift : Evidence from  $^{40}\text{Ar} / ^{39}\text{Ar}$  geochronology from the Sangre de Cristo Mountains , south-central Colorado and northern New Mexico. *Geol. Soc. Am. Spec. Pap.*, 47–64 (2002).
17. M. S. Ghiorso, B. W. Evans, Thermodynamics of rhombohedral oxide solid solutions and a revision of the Fe-Ti two-oxide geothermometer and oxygen-barometer. *Am. J. Sci.* **308**, 957–1039 (2008).
18. K. V. Cashman, R. Stephen, J. Sparks, How volcanoes work: A 25 year perspective. *Bull. Geol. Soc. Am.* **125**, 664–690 (2013).
19. T. Shea *et al.*, Textural studies of vesicles in volcanic rocks : An integrated methodology (2010), doi:10.1016/j.jvolgeores.2009.12.003.
20. A. Jambon, P. Lussiez, R. Clocchiatti, J. Weisz, J. Hernandez, Olivine growth rate in a tholeiitic basalt: An experimental study of melt inclusion in plagioclase. *Chem. Geol.* **96**, 277–287 (1992).

21. L. Wilson, J. W. Head, Review and Analysis and of Volcanic Eruption To Theory Relationships Landforms. *Rev. Geophys.* **32**, 221–263 (1994).
22. J. J. Papike, J. M. Karner, C. K. Shearer, P. V. Burger, Silicate mineralogy of martian meteorites. *Geochim. Cosmochim. Acta.* **73**, 7443–7485 (2009).
23. A. Ruzicka, G. a. Snyder, L. a. Taylor, Vesta as the howardite, eucrite and diogenite parent body: Implications for the size of a core and for large-scale differentiation. *Meteorit. Planet. Sci.* **32**, 825–840 (1997).
24. H. Yurimoto *et al.*, Origin and Evolution of Oxygen Isotopic Compositions of the Solar System. *Russell J. Bertrand Russell Arch.* **1**, 1–16 (2001).
25. U. W. Bläß, F. Langenhorst, C. McCammon, Microstructural investigations on strongly stained olivines of the chassignite NWA 2737 and implications for its shock history. *Earth Planet. Sci. Lett.* **300**, 255–263 (2010).
26. J. J. Papike, J. M. Karner, C. K. Shearer, Determination of planetary basal parentage: A simple technique using the electron microprobe. *Acta Metal.* **88**, 469–472 (2003).
27. S. Yang *et al.*, Siderophile and chalcophile element abundances in shergottites : Implications for Martian core formation. **24**, 1–24 (2015).
28. W. F. McDonough, S. s. Sun, The composition of the Earth. *Chem. Geol.* **120**, 223–253 (1995).
29. F. E. Jenner, H. S. C. O’Neill, Analysis of 60 elements in 616 ocean floor basaltic glasses. *Geochemistry, Geophys. Geosystems.* **13**, 1–11 (2012).
30. E. Jagoutz *et al.*, in *LPSC X* (1979), pp. 610–612.

31. N. L. Chabot, D. S. Draper, C. B. Agee, Conditions of core formation in the earth: Constraints from Nickel and Cobalt partitioning. *Geochim. Cosmochim. Acta.* **69**, 2141–2151 (2005).
32. A. J. V Riches *et al.*, Petrology and geochemistry of Yamato 984028: A cumulate lherzolitic shergottite with affinities to Y 000027, Y 000047, and Y 000097. *Polar Sci.* **4**, 497–514 (2011).
33. M. Miyahara, E. Ohtani, A. El Goresy, S. Ozawa, P. Gillet, Phase transition processes of olivine in the shocked Martian meteorite Tissint: Clues to origin of ringwoodite-, bridgmanite- and magnesiowustite-bearing assemblages. *Phys. Earth Planet. Inter.* **259**, 18–28 (2016).
34. J. Hu, T. G. Sharp, High-pressure phases in shock-induced melt of the unique highly shocked LL6 chondrite Northwest Africa 757. *Meteorit. Planet. Sci.* **51**, 1353–1369 (2016).
35. D. D. Bogard, D. H. Garrison, M. Norman, E. R. D. Scott, K. Keil,  $^{39}\text{Ar}/^{40}\text{Ar}$  age and petrology of Chico: Large-scale impact melting on the L chondrite parent body. *Geochim. Cosmochim. Acta.* **59**, 1383–1399 (1995).
36. T. Blackburn, C. M. O'D. Alexander, R. Carlson, L. T. Elkins-Tanton, The accretion and impact history of the ordinary chondrite parent bodies. *Geochim. Cosmochim. Acta.* **200**, 201–217 (2016).